



HAL
open science

New 3-D density maps of NaI and CaII interstellar absorption within 300pc

Barry Y. Welsh, Rosine Lallement, Jean-Luc Vergely, Séverine Raimond

► **To cite this version:**

Barry Y. Welsh, Rosine Lallement, Jean-Luc Vergely, Séverine Raimond. New 3-D density maps of NaI and CaII interstellar absorption within 300pc. *Astronomy and Astrophysics - A&A*, 2010, 510, pp.A54. 10.1051/0004-6361/200913202 . hal-00443652

HAL Id: hal-00443652

<https://hal.science/hal-00443652>

Submitted on 16 Jul 2020

HAL is a multi-disciplinary open access archive for the deposit and dissemination of scientific research documents, whether they are published or not. The documents may come from teaching and research institutions in France or abroad, or from public or private research centers.

L'archive ouverte pluridisciplinaire **HAL**, est destinée au dépôt et à la diffusion de documents scientifiques de niveau recherche, publiés ou non, émanant des établissements d'enseignement et de recherche français ou étrangers, des laboratoires publics ou privés.

New 3D gas density maps of NaI and CaII interstellar absorption within 300 pc^{★,★★}

B. Y. Welsh¹, R. Lallement², J.-L. Vergely³, and S. Raimond²

¹ Space Sciences Laboratory, University of California, 7 Gauss Way, Berkeley, CA 94720, USA
e-mail: bwelsh@ssl.berkeley.edu

² Université Versailles St-Quentin; CNRS/INSU, LATMOS-IPSL, BP 3, 91371 Verrières-le-Buisson, France

³ ACRI-ST, BP 234, 06504 Sofia-Antipolis, France

Received 28 August 2009 / Accepted 11 December 2009

ABSTRACT

Aims. We present new high resolution ($R > 50\,000$) absorption measurements of the NaI doublet (5889–5895 Å) along 482 nearby sight-lines, in addition to 807 new measurements of the CaII K (3933 Å) absorption line. We have combined these new data with previously reported measurements to produce a catalog of absorptions towards a total of 1857 early-type stars located within 800 pc of the Sun. Using these data we have determined the approximate 3-dimensional spatial distribution of neutral and partly ionized interstellar gas density within a distance-cube of 300 pc from the Sun.

Methods. All newly recorded spectra were analyzed by means of a multi-component line profile-fitting program, in most cases using simultaneous fits to the line doublets. Normalized absorption profiles were fitted by varying the velocity, doppler width and column density for all intervening interstellar clouds. The resulting total column densities were then used in conjunction with the Hipparcos distances of the target stars to construct inversion maps of the 3D spatial density distribution of the NaI and CaII bearing gas.

Results. A plot of the equivalent width of NaI versus distance reveals a wall of neutral gas at ~ 80 pc that can be associated with the boundary wall to the central rarefied Local Cavity region. In contrast, a similar plot for the equivalent width of CaII shows no sharply increasing absorption at 80 pc, but instead we observe a slowly increasing value of CaII equivalent width with increasing sight-line distance sampled. Low values for the volume density of NaI ($n_{\text{NaI}} < 10^{-9} \text{ cm}^{-3}$) are generally found within 50 pc of the Sun, whereas values in the range $10^{-8} > n_{\text{NaI}} > 10^{-10} \text{ cm}^{-3}$ are found for sight-lines with distance > 300 pc. Both high and low values of the volume density of CaII (n_{CaII}) are found for sight-lines < 30 pc, dependent on whether local gas cloudlets are encountered. For distances > 100 pc a value of $n_{\text{CaII}} \sim 10^{-9} \text{ cm}^{-3}$ is typical for most sight-lines, indicating that the distribution of CaII bearing gas is fairly uniform throughout the general ISM. Our three maps of the 3D spatial distribution of local neutral NaI absorption extend and improve upon the accuracy of similar maps initially presented by Lallement et al. (2003, A&A, 411, 447), with many new neutral interstellar gas features (such as low neutral density gas tunnels) in the local interstellar medium now being revealed for the first time. The maps of the 3D distribution of partially ionized CaII gas are the first of their kind to be presented and exhibit many spatial similarities to those of their equivalent NaI absorption maps. A major finding from both sets of maps is that the low density Local Cavity region is surrounded by a highly fragmented wall of higher density NaI and CaII gas clouds. The appearance of this broken boundary may be linked to the purported explosive origin of the Local Cavity. Maps of the distribution of CaII gas density reveal the presence of many partially ionized low density cloudlets that reside within the Local Cavity, and their newly derived 3D spatial contours confirm previous observations of the local gas by Redfield & Linsky (2008, ApJ, 673, 283). Both the NaI and CaII maps suggest that the Local Cavity may contain several low density sub-cavities that are surrounded by thin filaments of neutral and/or partially ionized gas. However, further observations will be required to confirm the existence of a collection of cell-like interstellar cavities. The new maps also reveal several sight-lines where CaII absorption is high and the corresponding NaI absorption is low, and vice-versa. Such regions are probably influenced by the effects of the local stellar ionization field which can significantly affect the observed NaI/CaII column density ratio. Plots of this ratio as a function of distance for stars located near to the galactic plane show values in the range 0.1 to 1.0 for sight-lines with distances < 80 pc. However, ratio values of between 0.5 and 20 are typical for more distant sight-lines. The highest values of the NaI/CaII ratio are found towards $l \sim 150^\circ$ in the direction of the Taurus dark clouds, with ratio values in the narrower range of 0.1 to 5 being found in galactic quadrant 3.

Key words. solar neighborhood – ISM: atoms – ISM: clouds

1. Introduction

Knowledge of the spatial distribution, dynamics and the associated physical and chemical state of interstellar gas can provide important insights into the subtle interplay between the evolution

of stars and their exchange of material to and from the ambient interstellar medium (ISM). Although much valuable work in this field has been achieved through numerous 21 cm radio and infrared surveys of our Galaxy, knowledge of the physical state and spatial distribution of the interstellar gas within 300 pc of the Sun is still far from complete. The low density region surrounding our Sun to ~ 100 pc in all directions is termed “the Local Cavity” (LC) and has been shown to be largely free of cold and dense gas, although it does contain many partially ionized diffuse cloudlets often referred to as “local fluff”

* Partly based on observations collected at the European Southern Observatory, La Silla, Chile.

** Full Table 1 is only available in electronic form at the CDS via anonymous ftp to cdsarc.u-strasbg.fr (130.79.128.5) or via <http://cdsweb.u-strasbg.fr/cgi-bin/qcat?J/A+A/510/A54>

(Redfield & Linsky 2008). The actual physical state of the gas that presumably fills the remaining volume in the Local Cavity is still much debated. The prevailing view is that it is mainly filled with a very low density, highly ionized (million K) gas, as inferred by observations of the diffuse soft X-ray (0.25keV) background emission (Snowden et al. 1998) and also by the detection of local absorption from the high ionization OVI (1032 Å) line by Savage & Lehner (2006). However, several authors have raised some serious arguments against the prevailing interpretation of these data, such that the LC gas may be of a far lower temperature or in a state far from ionization equilibrium (Breitschwerdt 2001; Koutroumpa et al. 2007; Barstow et al. 2009). Based on the demonstration that most of the unabsorbed soft X-ray brightness at low galactic latitudes is actually solar wind charge-transfer X-ray emission generated within the heliosphere, Koutroumpa et al. (2009) have suggested that the LC may contain far cooler or more tenuous gas at low altitudes ($|z| < 60\text{--}100$ pc) with the soft X-ray emission seen from $|b| > 30^\circ$ arising from an “external” hot gas and from the overlying halo (Welsh & Shelton 2009).

Our unique placement within this low density interstellar cavity allows us to directly measure its spatial extent and physical state through high spectral resolution absorption measurements that are mostly uncontaminated by intervening dense line-of-sight interstellar features. Over the past 20+ years we have been carrying out high spectral resolution ($R \sim 100\,000$) absorption observations of the local neutral and partially ionized interstellar gas using both the NaI D-line doublet at 5890 Å and the CaII-K line at 3933 Å (Lallement et al. 1986; Vallerga et al. 1993; Welsh et al. 1994; Sfeir et al. 1999; Lallement et al. 2003). These, and many other, observations have allowed us to construct a picture of the distribution of neutral gas in the local ISM in which the LC is connected through interstellar tunnels to other surrounding cavities, as predicted in the model of the ISM by Cox & Smith (1974). In particular, maps of the distribution of NaI absorption have revealed 3 large interstellar features that dominate the appearance of the local ISM within 200 pc. These are: (i) the 50 pc diameter and 200 pc long extension to the LC in the direction of the star β CMa (Welsh 1991); (ii) the extension of the rarefied LC into the lower galactic halo to form an open-ended Local Chimney feature (Welsh et al. 1999); and (iii) the apparent connection of the LC with the large Loop I superbubble at a distance of ~ 80 pc (Welsh & Lallement 2005). We attribute the name “Loop 1 superbubble” to the cavity centered at longitude 345 deg, although the link between this cavity and the radio feature is far from well understood. It seems likely that the existence of these 3 features is somehow linked to the formation history of the LC itself.

The need for accurate maps of the 3D density distribution of neutral local gas has been demonstrated in wide variety of recent studies (Oegerle et al. 2005; Smith et al. 2005; Combet et al. 2005; Posselt et al. 2007; Wolleben 2007). Such maps are particularly relevant for studying the interaction regions between local gas residing in the galactic plane, gas in adjacent interstellar cavities and local gas being ejected into, and falling from, the lower galactic halo. It is important to note that *only* when absorption data are combined with parallax measurements can the distances to gas clouds be accurately derived. Maps of the distribution of interstellar gas derived from HI, CO and the IR are of two-dimensions and cannot provide accurate distance estimates to gas clouds. Even so, the accuracy and spatial extent of our existing absorption maps are presently limited by (a) the number of sight-line directions sampled; (b) the sampling

length along and between each sight-line and (c) the distance over which each sight-line extends. At present the most accurate maps of the density distribution of local neutral gas are those presented by Lallement et al. (2003). Some 1005 sight-lines within ~ 250 pc were observed using NaI absorption in order to produce 3D neutral gas density distribution maps to a distance of ~ 150 pc in most directions. The galactic distribution of these 1005 sight-lines is shown in Fig. 1 of Lallement et al. (2003), hereafter Paper I. Many of these observations traced the extent of Gould’s Belt, since only early-type stars were used as background absorption sources. We note that in Paper I the typical global sampling area on the sky was ~ 1 target per 50 sq. deg, with significantly less coverage at high galactic latitudes.

No equivalent maps of the density distribution of partially ionized gas, as traced by the interstellar CaII absorption line, currently exist for the local ISM. This is particularly important for sight-lines $\lesssim 80$ pc, since the LC gas is thought to mainly exist in an ionization state higher than that which can be probed by the NaI ion (Welsh et al. 1994). Many diffuse and partly ionized cloudlets are known to exist within this volume and previous studies have demonstrated that the CaII K-line is an excellent tracer of absorption of this physical phase of the local gas (Lallement et al. 1986; Crawford et al. 1997). In fact, in a comparison study of high resolution ground-based CaII K-line and UV (FeII and MgII) absorption line data towards stars within 100 pc by Redfield & Linsky (2002), it was found that most (but not all) sight-line components were observed in both the CaII and UV lines to within a velocity error of only ± 1.5 km s $^{-1}$. This evidence suggests that the CaII line is a good indicator of the absorption structure that one might expect from the warm and ionized gas sampled by the UV lines. The good agreement between these absorption velocities clearly suggests a collocation for the formation of both the optical and UV lines within these same warm and diffuse local gas clouds. Furthermore, UV observations of stars within the β CMa interstellar tunnel suggest that although the neutral gas density along this 200 pc long interstellar feature may be very low, this is not the case for ionized gas components (Dupin & Gry 1998). Clearly it would be instructive to compare maps of the spatial distribution of CaII absorption (which is sensitive to partially ionized gas) and those derived from NaI observations (which trace cold and neutral gas) for the local ISM.

In this paper we report on the results of an extended survey of NaI and CaII absorption lines recorded at high spectral resolution ($R > 50\,000$) towards many newly observed early-type stars mostly located within 800 pc of the Sun. We present new absorption measurements of the NaI doublet recorded along 482 sight-lines, in addition to 807 new measurements of CaII absorption along 807 sight-lines. When added to similar NaI and CaII absorption measurements reported in the literature, we are now able to present new maps to 300 pc of the 3D distribution of neutral and partially ionized gas towards 1678 stars (at NaI) and 1267 stars (at CaII). Although these new data confirm many of the findings of Paper I, they also show several new interstellar gas features now revealed through the increased level of sampling of local ISM sight-lines, especially at high galactic latitudes and in regions with distances in the 150–350 pc regime. The 3D maps of local CaII absorption are the first of their kind to be presented, and in several respects they mimic many of the interstellar features seen in the equivalent maps of local NaI absorption. However, there are a significant number of regions where CaII absorption is high and NaI absorption is low, and vice-versa. Such variations in the observed column density ratio of $N(\text{NaI})/N(\text{CaII})$ are influenced by the conditions

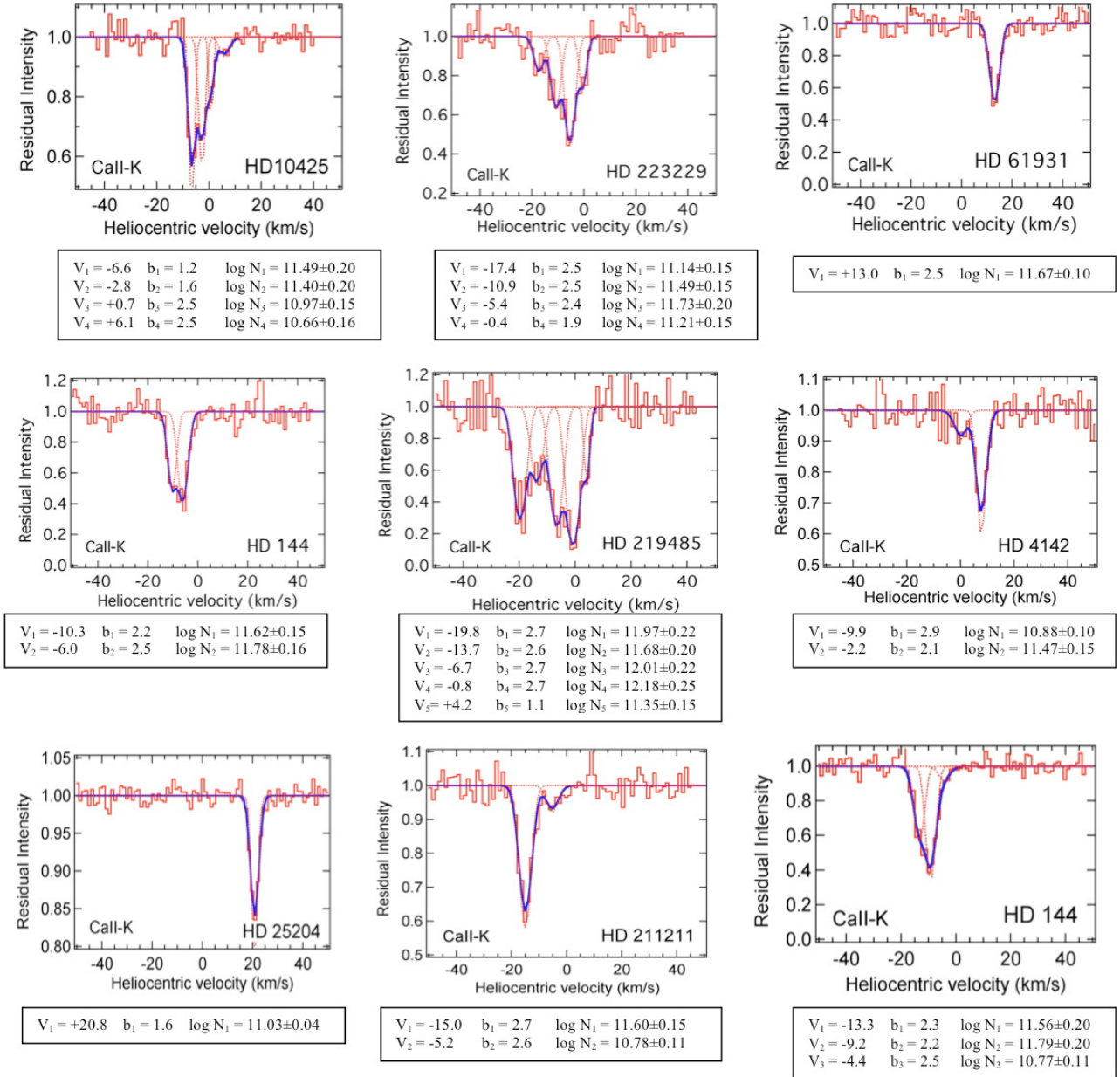


Fig. 1. Examples of interstellar CaII-K line absorption profiles together with best-fit models (thick line) recorded with the Aurelia spectrograph on the 1.52 m telescope at the Observatoire de Haute Provence. Dotted lines are the model components prior to instrumental convolution. The best-fit component values of velocity (V), doppler-width (b) and column density (N) are listed in the box beneath each profile.

in the local stellar ionization field. Values of this ratio for stars near to the galactic plane in each of the 4 galactic quadrants are also presented. Finally, as a by-product to determining the (NaI and CaII) gas column densities along each sight-line we have also determined the absorption velocity (i.e. cloud component) structure towards each target. These results will be published in a separate paper that deals with the kinematics of local gas clouds within ~ 150 pc (Lallement et al. 2010).

2. Observations and data reduction

We present observations of both the interstellar NaI D-line doublet at ~ 5890 Å and the CaII K-line at 3393 Å recorded in the absorption spectra of early-type stars with distances < 0.8 kpc. These data were obtained during observing runs performed

over the period 2003–2008 using the following instrumentation (i) the Aurelie spectrograph at the 1.52 m telescope of the Observatoire de Haute Provence (France); (ii) the Hamilton echelle spectrograph on the 0.9 m coude feed telescope at the Lick Observatory (USA); (iii) the Hercules echelle spectrograph on the 1.0 m McLellan telescope at the Mt. John Observatory (New Zealand); (iv) the FEROS coude echelle spectrograph on the 2.2 m telescope at the European Southern Observatory (Chile) and (v) the GIRAFFE fiber-fed echelle spectrograph at the 1.9 m Radcliffe telescope of the South African Astronomical Observatory (RSA). The spectral resolution for these interstellar data was 3 km s^{-1} for the Observatoire de Haute Provence (OHP) data, 5 km s^{-1} for the Lick Observatory data, 4 km s^{-1} for the Mt. John Observatory (MJO) data, 6 km s^{-1} for the FEROS ESO data and 7.5 km s^{-1} for the South African Astronomical Observatory (SAAO) data.

Table 1. NaI and CaII absorption measurements.

| Star _{HD} | l | b | distance (pc) | W_λ (D2) m(Å) | W_λ (D1) m(Å) | $\log N(\text{NaI})_{\text{TOT}}$ cm ⁻² | Reference (NaI) | W_λ (K) m(Å) | $\log N(\text{CaII})_{\text{TOT}}$ cm ⁻² | Reference (CaII) |
|--------------------|-----|-------|------------------|--------------------------|--------------------------|---|--------------------|-------------------------|--|---------------------|
| 179029 | 0.1 | -20 | 318 | 124.3 | 105.4 | 12.37 | ESO-2007 | 53 | 12.01 | ESO-2007 |
| 157056 | 0.5 | 6.6 | 173 | 87.0 | | 11.98 | (1) | 38.0 | 11.67 | (2) |
| 172016 | 0.8 | -12.5 | 225 | 136.6 | 76.20 | 11.97 | ESO-2007 | 25.7 | 11.33 | ESO-2007 |
| 195599 | 0.9 | -36.1 | 186 | <2.5 | | <10.15 | ESO-2007 | 3 | 10.65 | ESO-2007 |
| 203006 | 1.2 | -45.0 | 57 | | | | | <5 | <10.4 | (3) |
| 171034 | 1.3 | -11.0 | 685 | 240.0 | 175.0 | 12.39 | MJO-2007 | 83.4 | 12.06 | MJO-2007 |
| 152909 | 1.6 | 14.4 | 209 | 235.0 | 198.5 | 12.83 | ESO-2006 | 104.9 | 12.24 | ESO-2006 |
| 154204 | 1.9 | 12.4 | 122 | 179 | 142 | 12.66 | (4) | | | |
| 164019 | 1.9 | -2.6 | 556 | | | | | 498 | 12.99 | (5) |
| 161756 | 2.0 | 0.5 | 348 | 284.8 | 236.6 | 12.87 | ESO-2006 | 99.9 | 12.30 | ESO-2006 |
| 145570 | 2.5 | 28.8 | 51 | 6.7 | 6.1 | 10.67 | ESO-2008 | 21.9 | 11.52 | ESO-2008 |
| 158643 | 2.5 | 5.3 | 131 | | | 11.05 | (6) | 20.3 | 11.26 | (7) |
| 165365 | 2.8 | -3.7 | 418 | 186.4 | 121.8 | 12.15 | ESO-2008 | 58.3 | 11.91 | ESO-2008 |
| 180885 | 2.8 | -20.7 | 565 | 109.8 | 86.7 | 12.16 | MJO-2006 | | | |
| 197630 | 2.9 | -38.3 | 98 | 12.9 | 3.3 | 10.71 | MJO20-06 | 10.3 | 11.06 | MJO-2007 |
| 151884 | 3.2 | 17.4 | 268 | 372.8 | 348.9 | 12.89 | ESO-2008 | 131.8 | 12.38 | ESO-2008 |
| 45607 | 3.9 | 29.7 | 77 | 30.0 | 15.0 | 11.28 | (8) | 17.6 | 11.36 | LICK-2007 |
| 141378 | 4.1 | 37.3 | 49 | <3 | | <10.3 | (9) | | | |
| 141569 | 4.2 | 36.9 | 99 | | | 12.66 | (10) | | 11.65 | (10) |
| 188113 | 4.2 | -27.8 | 446 | 199.5 | 152.6 | 12.50 | ESO-2008 | 66.9 | 12.0 | ESO-2008 |

Notes. The full table is only available in electronic form at the CDS.

Interstellar sight-lines were generally selected using the criteria that the background stellar targets possess: (i) a Hipparcos catalog distance (ESA 1997) normally less than 400 pc and with an associated relative standard parallax error smaller than 0.3 (however several targets with distances up to 800 pc were also included for certain sight-lines of specific interest); (ii) a spectral type earlier than A5V; (iii) a stellar rotational velocity $>25 \text{ km s}^{-1}$; (iv) a galactic position that filled in areas of the sky not well sampled by the targets listed in Paper I; and (v) a sufficiently bright visual magnitude that a well-exposed spectrum could be gained within a 60 min exposure. We also avoided observations of known spectroscopic binary stars, since interstellar features are often difficult to identify within their stellar absorption profiles. In Table 1, available on the CDS, we list information on the newly observed targets that includes their HD number, galactic longitude and latitude, Hipparcos distance (in pc) and the observatory (OHP, Lick, MJO, ESO and SAAO) where the data was taken, together with the year of observation.

All of the data, except for the MJO and ESO observations, were reduced using software routines outlined in detail in Sfeir et al. (1999). These routines involve: (i) division of the raw data by a flat-field; (ii) removal of instrumental background light and cosmic rays; (iii) removal of telluric water vapor lines (which particularly affect the NaI D2-line at $\lambda 5890 \text{ \AA}$) using either a synthetic telluric transmission spectrum as detailed in Lallement et al. (1993) or by division by a purely stellar-atmospheric absorption spectrum of an unreddened (nearby) B star observed at a similar altitude and time; and (iv) spectral order extraction and wavelength calibration using Th-Ar lamp spectra recorded several times throughout each observing night. Similar data reduction processes were performed on the Mt. John Observatory and ESO data using their own in-house standardized echelle data extraction software packages.

The wavelength calibrated spectral data were subsequently fit with a high order polynomial in order to define a local stellar continuum placement, such that the equivalent widths (W_λ) of the NaI and CaII absorption lines could be measured from these resultant intensity profiles. The errors on the measured values of W_λ are dominated by the statistical uncertainty on the

measured counts within each line profile and the systematic uncertainty in the local continuum placement (see Welsh et al. 1990, for a fuller discussion). These two sources of error are added in quadrature to derive the measurement error. Typically, for a well-exposed spectrum, a measurement error of $\sim 5\%$ is normal for our data. Upper limits to the value of equivalent width where no absorption line was detected with significance were derived from conservative estimates of the strength of a potential absorption feature appearing at a level $>2.5\text{-}\sigma$ above the rms value of the local continuum. For the majority of our well-exposed spectra (i.e. $S/N > 30:1$) this typically resulted upper limit values of $W_\lambda < 2.5 \text{ m\AA}$ for both the NaI-D2 and CaII-K lines. The measured values of W_λ for the NaI (D2 & D1) and the CaII-K lines are listed in Table 1 for our presently observed sight-lines.

For the majority of targets with distances $\lesssim 300 \text{ pc}$ both the interstellar NaI and CaII absorption lines are not greatly saturated. Thus, we were able to accurately fit these profiles with absorption components (i.e. gas clouds) using the line-fitting procedure described in Sfeir et al. (1999). A best-fit theoretical absorption profile is generated that is characterized by 3 parameters: (i) an interstellar cloud (heliocentric) velocity; V (ii) a doppler velocity dispersion parameter (b -value) and (iii) a cloud component column density, $N(\text{NaI})$ or $N(\text{CaII})$. The best-fit models were further constrained by fitting *both* of the NaI D-lines simultaneously (with the fit being biased towards the stronger D2 line). For the ESO data, in which both the CaII K and H-lines were available, the best-fit for the doublet was similarly constrained.

As an indication of the quality of the data recorded with the spectrograph+telescope systems at each of the 5 observatories, in Figs. 1–5 we show some typical model fits to the observed interstellar NaI and CaII absorption profiles recorded towards stars with distances in the 50–500 pc range. The best-fit model parameters (i.e. V , b and $N(\text{NaI})$ and/or $N(\text{CaII})$) for the (several) cloud components required to fit each of these absorption profiles are listed in a box beneath each of the profiles in these figures. The fits were performed using the minimum number of absorption components, with the addition of extra components only being

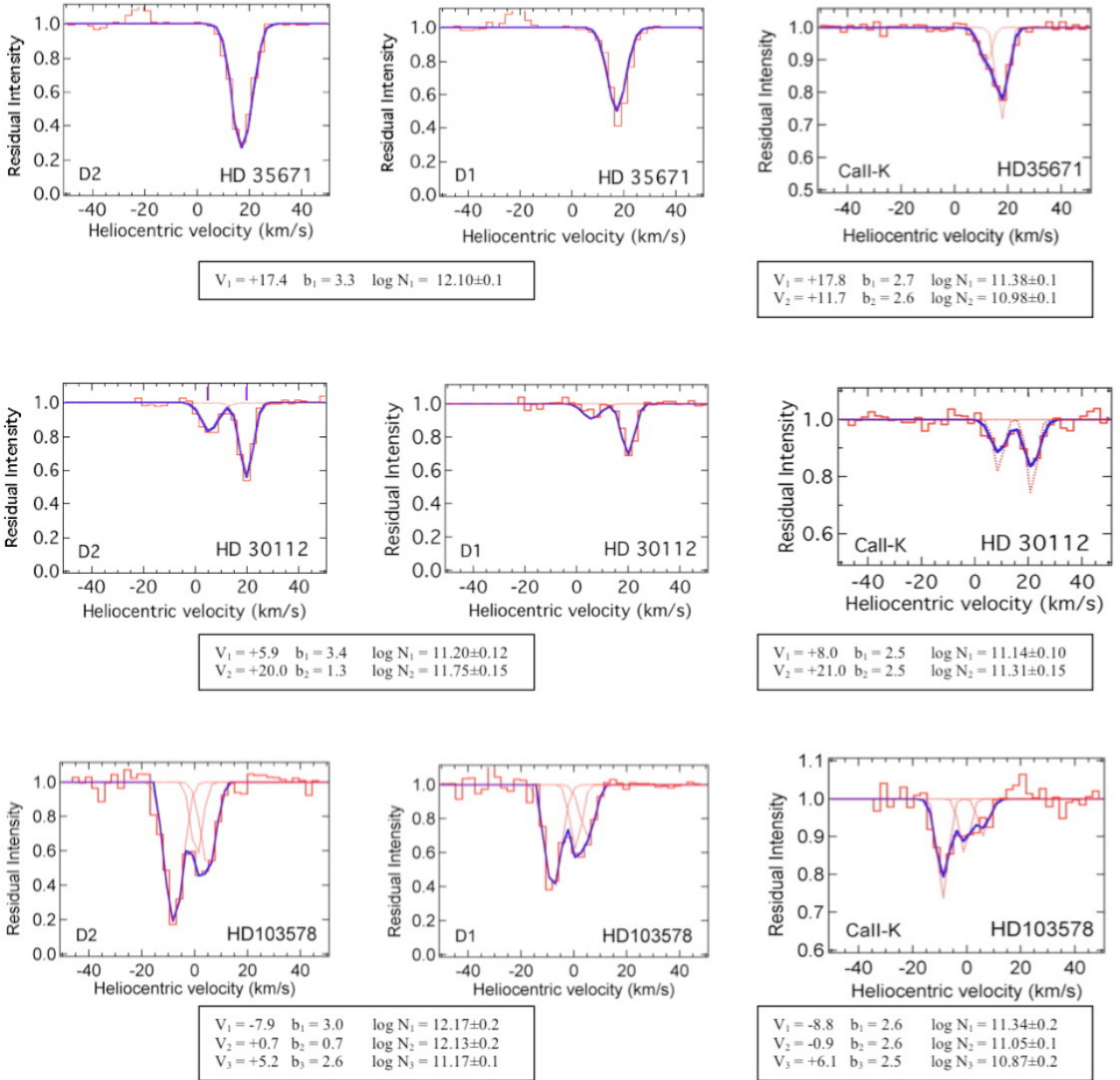


Fig. 2. Examples of interstellar NaI D2 and D1 and CaII-K line absorption profiles together with best-fit models (thick line) recorded with the Hamilton spectrograph on the 0.9 m CAT telescope at the Lick Observatory of the University of California. Dotted lines are the model components prior to instrumental convolution. The best-fit component values of velocity (V), doppler-width (b) and column density (N) are listed in the box beneath each profile.

deemed necessary until the residual between the model fit and the data points was approximately equal to the rms error of the data. In general (dependent on the spectrograph used), the accuracy of the placement of each of the cloud component velocities within these line-fits is $\sim \pm 0.5 \text{ km s}^{-1}$.

The highest resolution data (see Fig. 1) was obtained for the CaII K-line at the OHP, and hence it is no surprise that these data generally require more absorption components to fit the observed profiles. In contrast, the data gained with the lower resolution FEROS system on the 2.2 m telescope (shown in Fig. 4) is of the highest S/N ratio and allows access to both the NaI and CaII doublets, such that the model fits can generally be constrained to a better degree of confidence. However, for the purposes of our present interstellar study we only require use of

the total equivalent width, $W_\lambda(\text{D2})$ and $W_\lambda(\text{K})$, and the summed total column density values, $N(\text{NaI})_{\text{tot}}$ and $N(\text{CaII})_{\text{tot}}$, measured towards each star. These values are listed in Table 1. The best-fit values of NaI and CaII column density for each cloud component for all of the newly observed targets will be presented in a forthcoming paper which will concentrate of the velocity structure of the local ISM within 150 pc (Lallement et al. 2010).

In order to increase the spatial sampling of interstellar gas absorption in the local ISM, in addition to the newly obtained data listed in Table 1 we have also included NaI and CaII interstellar measurements (of equivalent width and associated total column density) towards sight-lines $< 800 \text{ pc}$ that have been previously published in the literature. The corresponding data for each of these observations are also listed in Table 1 along

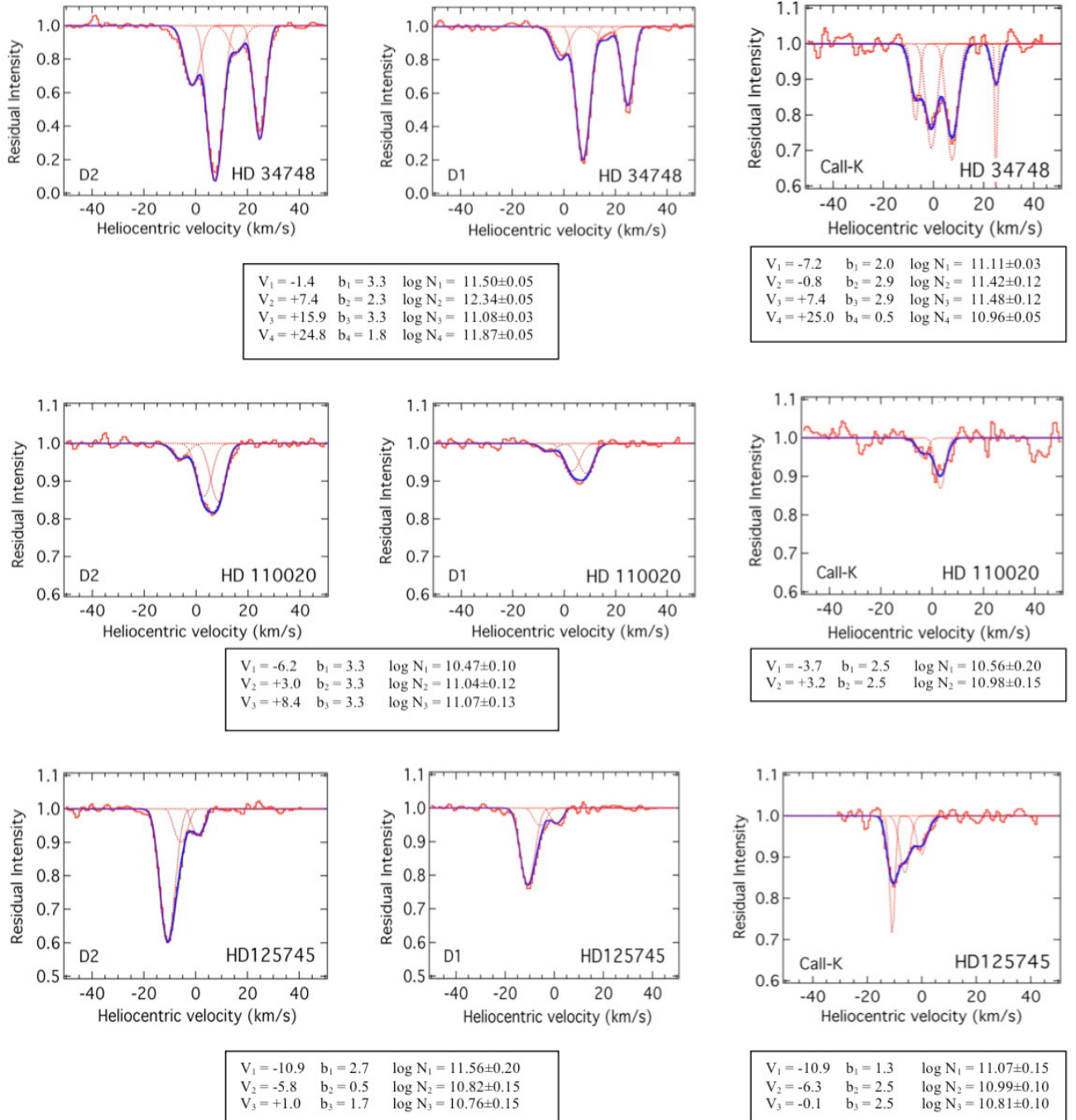


Fig. 3. Examples of interstellar NaI D2 and D1 and CaII-K line absorption profiles together with best-fit models (thick line) recorded with the Hercules spectrograph on the 1.0 m telescope at the Mt. John Observatory in New Zealand. Dotted lines are the model components prior to instrumental convolution. The best-fit component values of velocity (V), doppler-width (b) and column density (N) are listed in the box beneath each profile. The short vertical lines above some profiles indicate the position of the absorption component's velocity.

with the appropriate reference for the particular observation. For cases in which only values of equivalent width are quoted in the literature, we have derived a corresponding value of total column density (reported in Table 1) using empirical curves of growth for both NaI and CaII derived from all of the other data. We have not included interstellar data for targets with known (or suspected) circumstellar gas, since this can provide a significant (and variable) contribution to the values of NaI and CaII column density (Welsh et al. 1998). One important case of this type

is the star HD 225132 (2 Cet), which appeared in the NaI maps of Paper I as a nearby ($d = 70$ pc) condensation of cold gas lying within the confines of the LC. Recent high resolution measurements of NaI and CaII absorption by Redfield et al. (2007), which have subsequently been confirmed by our own measurements, revealed a far smaller value of NaI column density for this sight-line compared to that reported in Welsh et al. (1994). In addition, our own CaII measurements reveal a component at $V = +20$ km s⁻¹ not seen by Redfield et al. We have therefore

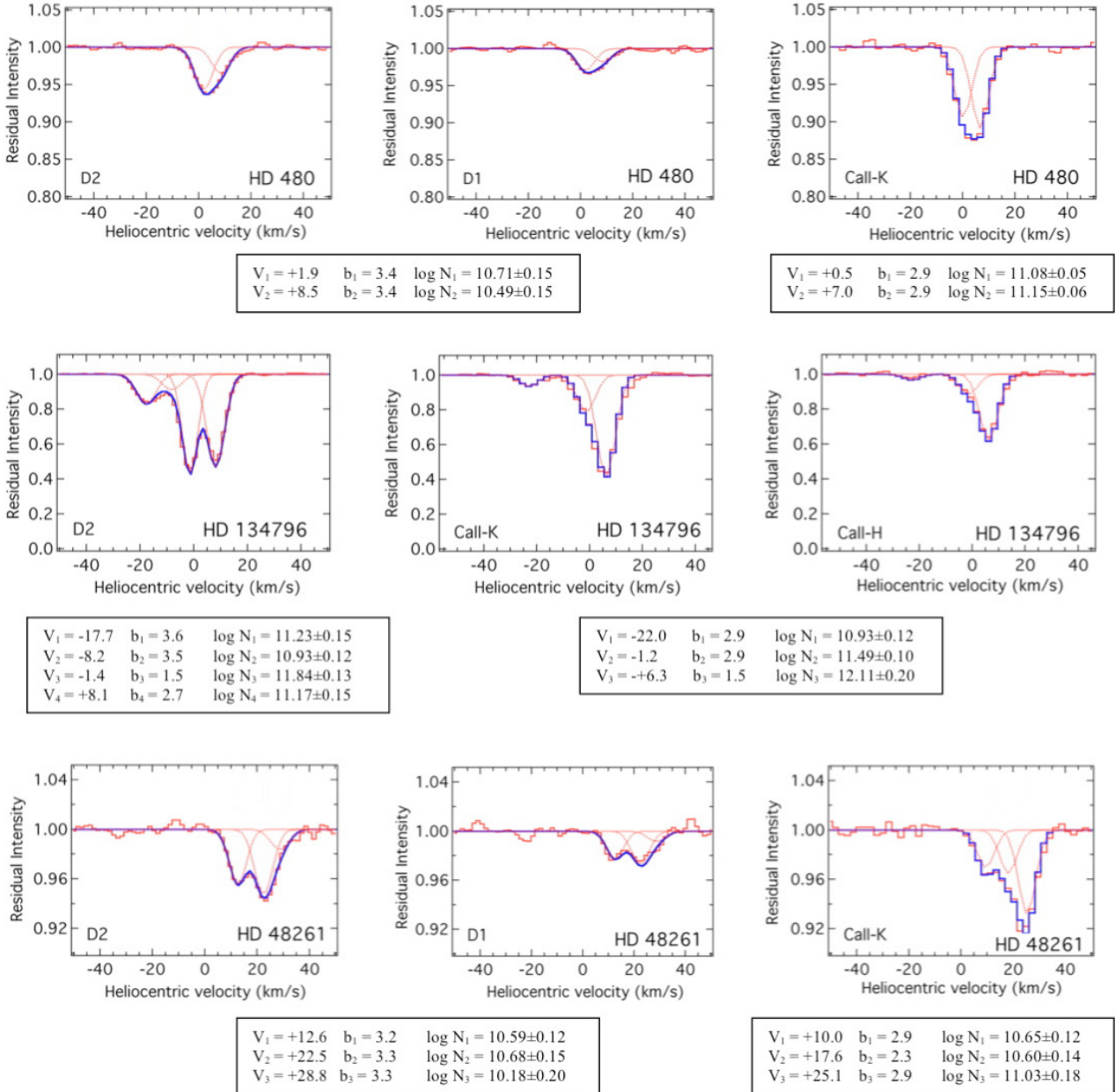


Fig. 4. Examples of interstellar NaI D2 and D1 and CaII K and H-line absorption profiles together with best-fit models (thick line) recorded with the FEROS spectrograph on the 2.2 m telescope at the European Southern Observatory in Chile. Dotted lines are the model components prior to instrumental convolution. The best-fit component values of velocity (V), doppler-width (b) and column density (N) are listed in the box beneath each profile.

removed this star from our compilation in Table 1. In total we now present 1678 NaI and 1267 CaII interstellar sight-line absorption measurements, 1088 of which have common sight-line measurements for both of these ions.

In Figs. 6a and b we show the galactic distribution of the respective 1678 NaI and 1267 CaII sight-lines sampled. Although the sky-coverage is significantly increased since Paper I, we note some areas of the sky (e.g. $l = 295^\circ$, $b = -45^\circ$ and $l = 160^\circ$, $b = -75^\circ$) remain sparsely sampled. This is primarily due to the paucity of suitably bright O, B and A-type stellar targets in these directions that can be observed in a reasonable exposure time with the presently available instrumentation. Therefore any conclusions derived from the mappings of interstellar absorption towards both of these galactic directions must be viewed with some caution. We also note that our selection of suitable targets

is biased against heavily reddened and visually faint ($m_v \gtrsim 6.5$) sight-lines, due to the practical restriction of \sim one hour of exposure time per recorded spectrum.

3. Interstellar absorption mapping

The measurements of NaI and CaII equivalent width and column density measured along the 1857 sight-lines allows us to probe the absorption characteristics of both neutral and partially ionized local interstellar gas. Our underlying assumption is that the NaI ion is a good tracer of the total amount of neutral and cold ($T < 1000$ K) interstellar gas along most galactic sight-lines (Hobbs 1978). Similarly, the CaII ion is assumed to trace both neutral and warmer ($T \leq 10\,000$ K) partially ionized gas clouds. Previous high resolution studies of NaI and CaII absorption

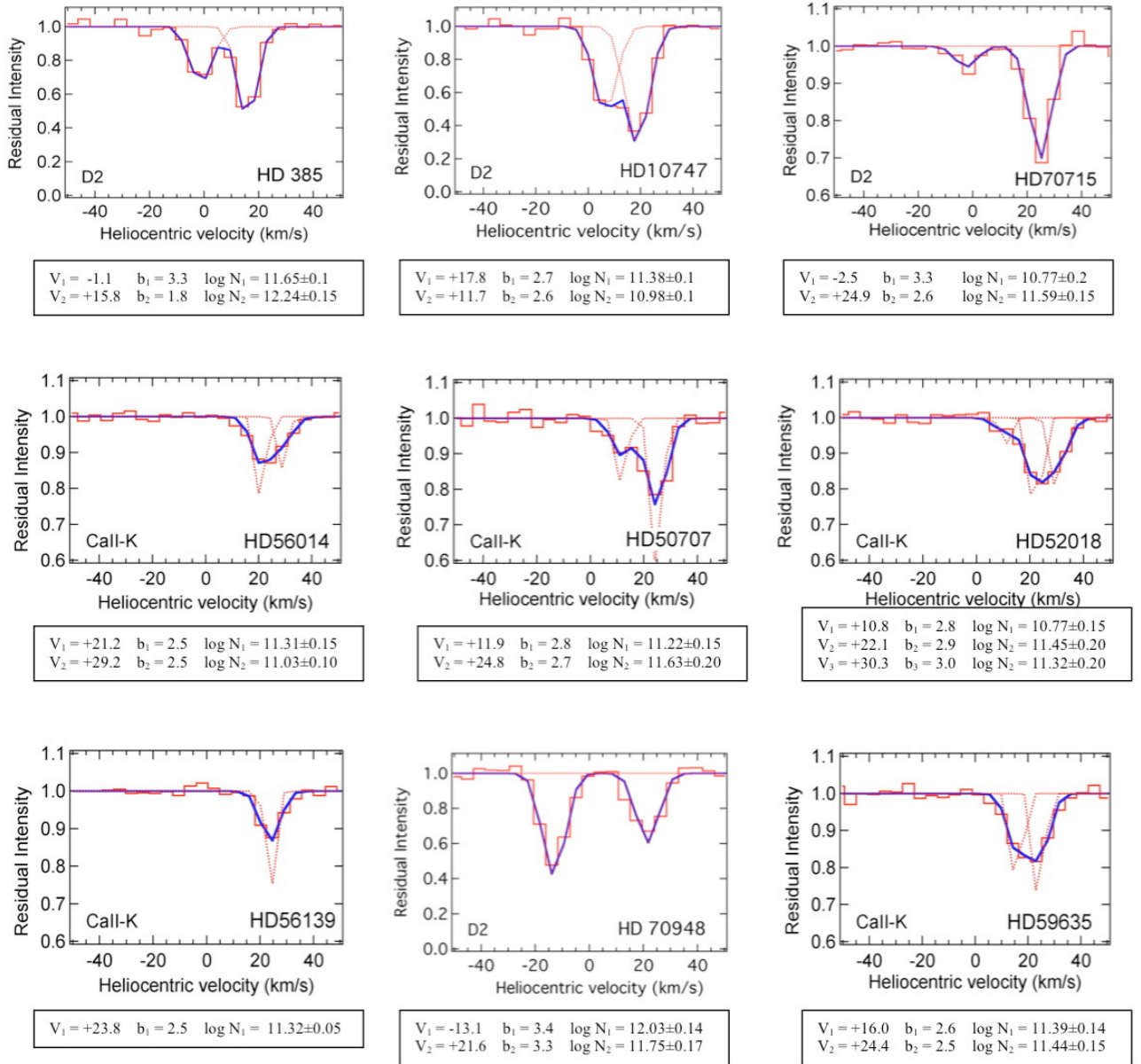


Fig. 5. Examples of interstellar NaI D2 and D1 and CaII-K line absorption profiles together with best-fit models (thick line) recorded with the GIRAFFE spectrograph on the 1.9 m telescope at the South African Astronomical Observatory. Dotted lines are the model components prior to instrumental convolution. The best-fit component values of velocity (V), doppler-width (b) and column density (N) are listed in the box beneath each profile.

suggest that the latter ion has larger absorption line-widths for components seen in NaI absorption at the same velocity (Welty et al. 1996). This has been interpreted as the CaII gas components occupying a larger volume than those of NaI, with an associated higher temperature and/or more turbulent velocity than the volume of gas occupied by NaI. In our present study, in which we average the absorption properties of gas along many interstellar sight-lines, we assume that the derived spatial distributions of both NaI and CaII are directly comparable. We note that CaII absorption not only arises in cold (and relatively dense) gas in which Ca may be heavily depleted onto dust grains and is the dominant ionization state, but it can also be present in warmer and lower density gas clouds where Ca is less depleted and in which CaII is a trace ionization state.

Our primary aim in this paper is to determine the 3D spatial distribution of interstellar gas (as characterized by NaI

and CaII absorption) to a distance of ~ 300 pc from the Sun. Following our previous work on this subject (Sfeir et al. 1999; Lallement et al. 2003), we produce plots of the spatial distribution of gas based on the inversion of column densities using a method originally devised by Vergely et al. (2001). This method of plotting, together with some of its advantages and shortcomings, has been described fully in Lallement et al. (2003). However, before presenting such gas density maps we firstly discuss the measurements of the equivalent widths of the interstellar NaI and CaII lines.

3.1. NaI and CaII equivalent width values

In Fig. 7 we show a plot of distance versus the total equivalent width of the NaI D2-line, $W_{\lambda}(D2)$, for targets with distances

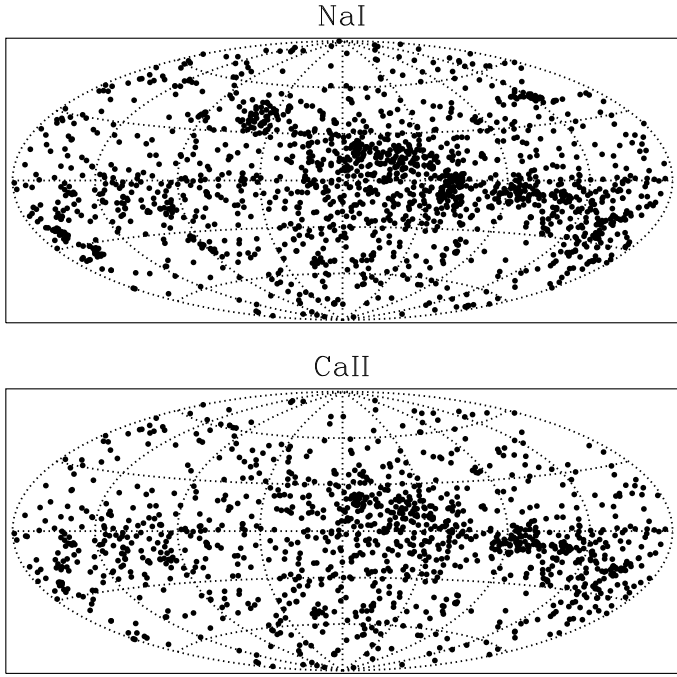


Fig. 6. Galactic distribution of the interstellar sight-lines sampled by a) NaI absorption, and b) CaII absorption. Both plots are centered at galactic co-ordinate (0, 0).

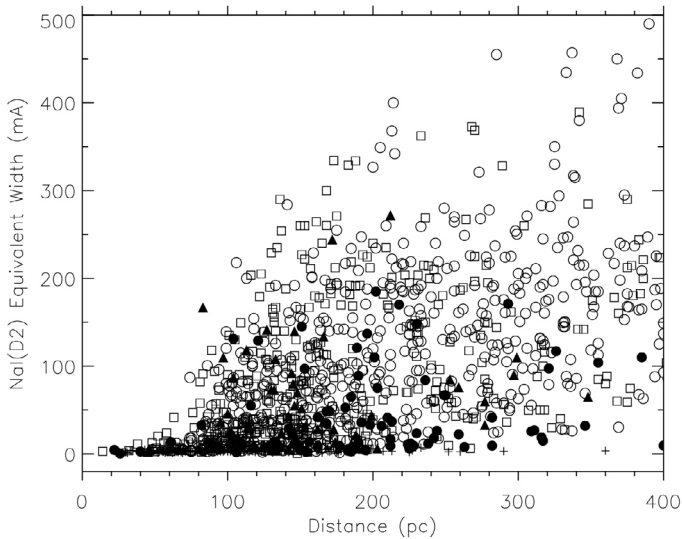


Fig. 7. Plot of the equivalent width ($\text{m}\text{\AA}$) of the interstellar NaI D2-line for stars with distances <400 pc. Filled triangles are for sight-lines with galactic latitude $b > +45^\circ$, open squares for sight-lines with $b = 0$ to 45° , open circles for sight-lines with $b = 0$ to -45° and filled circles for sight-lines with $b < -45^\circ$. Crosses are upper limit values. Note the sharp increase in the level of NaI absorption at ~ 80 pc, which is due to the neutral wall to the Local Cavity.

<400 pc. Note that this plot does not include sight-lines that have reported values of $N(\text{NaI})$, but no associated information on the measured equivalent width. This figure, in agreement with a similar plot shown in Sfeir et al. (1999), shows that very little measurable NaI absorption can be detected for distances (in all galactic directions) up to ~ 80 pc from the Sun. This general lack of appreciable NaI absorption ($W_\lambda(\text{D2}) \lesssim 5 \text{ m}\text{\AA}$) provides clear evidence that the volume of the LC is essentially free of major condensations of cold and dense neutral interstellar gas.

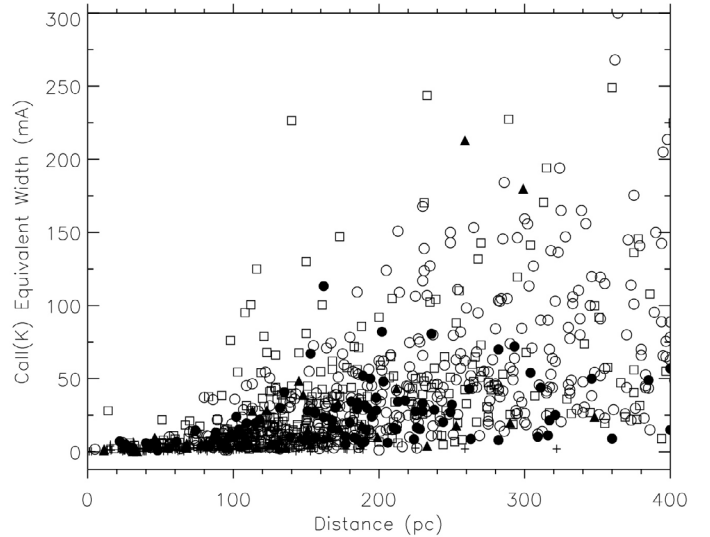


Fig. 8. Plot of the equivalent width ($\text{m}\text{\AA}$) of the interstellar CaII K-line for stars with distances <400 pc. Symbols are the same as those in Fig. 7.

Beyond ~ 80 pc the level of NaI absorption rises sharply over a short distance of ~ 20 pc to reveal the presence of a dense “wall” of neutral gas ($W_\lambda(\text{D2}) > 20 \text{ m}\text{\AA}$) that surrounds the LC in many galactic directions (Welsh et al. 1994). Beyond the LC neutral boundary, which is normally characterized by a single narrow velocity component in the NaI absorption profiles, more and more NaI absorbing (cold) neutral interstellar clouds are encountered as sight-line distances increase. In several galactic directions with distances >300 pc the NaI D-lines become increasingly saturated and we therefore generally see a slower increase in equivalent width value with greater distance sampled. However, we also note the presence of several sight-lines with distances >250 pc that have minimal associated NaI absorption (plotted as open circles in Fig. 7). These are sight-lines which extend into the lower galactic halo through the openings of the Local Chimney, a region of known low neutral gas density (Crawford et al. 2002). The nearest stars with distances less than 65 pc, but with “anomalously high” values of $W_\lambda(\text{D2}) > 10 \text{ m}\text{\AA}$, are HD 184006 ($d = 38$ pc), HD 159170 ($d = 48$ pc), HD 186882 ($d = 52$ pc), HD 105850 ($d = 56$ pc), HD 96819 ($d = 58$ pc) and HD 129685 ($d = 63$ pc).

In contrast with studies of interstellar NaI, previous investigations of CaII absorption have shown that the local ISM is composed of many diffuse and partially ionized warm ($T \sim 7000$ K) cloudlets that possess a complex velocity structure, even over distances as short as 5 pc (Crawford et al. 1998; Lallement et al. 1986). These cloudlets are randomly scattered within 50 pc of the Sun and although are generally not revealed by NaI absorption measurements, they have been extensively studied at ultraviolet wavelengths (Redfield & Linsky 2008). In Fig. 8 we show that the behavior of CaII absorption as a function of distance (to 400 pc) does not follow the same pattern that was found in Fig. 7 for NaI measurements. For the majority of sight-lines within ~ 100 pc we mostly find $W_\lambda(\text{CaII-K}) < 15 \text{ m}\text{\AA}$, with no sharply increasing value of absorption at ~ 80 pc that might feasibly be associated with the presence of gas associated with the boundary wall to the LC. Instead there seems to be a wide-spread local distribution of partially ionized CaII regions with a range of low integrated CaII absorption strengths that extends to at least 100 pc. Beyond ~ 100 pc we observe a slowly increasing

value of $W_\lambda(\text{CaII-K})$ with the sight-line distance sampled. Even by 200 pc there are still several sight-lines in which very little ($<3 \text{ m}\text{\AA}$) interstellar CaII is present. At a distance of ~ 300 pc a value of $W_\lambda(\text{CaII-K}) < 100 \text{ m}\text{\AA}$ is typical for most of the galactic directions sampled, although values in excess of 200 mÅ are found for a few higher density regions.

Welsh et al. (1997) have presented plots of the total column density of CaII versus the total column density of neutral HI which show that both quantities are broadly correlated. However, there is significant scatter in this relationship due to the fact that along any given interstellar line-of-sight the measured amount of CaII-bearing gas is closely linked to the ambient ionization conditions, the amount of dust depletion and the size and number of gas clouds encountered. The Local Cavity is an anomalous region of interstellar space that contains many randomly scattered warm and partially ionized low column density CaII-bearing cloudlets (each of $W_\lambda(\text{CaII-K}) \sim 5 \text{ m}\text{\AA}$, Redfield & Linsky 2002), probably mostly of similar physical size. Based on our fitting of CaII absorption profiles for stars <100 pc, the number of “cloudlets” encountered along a typical interstellar sight-line is generally <4 . Thus, the presently measured total equivalent width of CaII along sight-lines <100 pc is small ($<15 \text{ m}\text{\AA}$) and variable, dependent on the number of warm clouds encountered. For cold interstellar clouds that exist beyond the rarefied Local Cavity, it is generally assumed that the warm CaII gas is present in the “outer-skins” of these clouds (Vallerga et al. 1993; Welty et al. 1996). Thus, although the neutral wall boundary to the LC may contain significant amounts of cold NaI gas compared with sight-lines lying within the LC, the corresponding increase in the equivalent width of CaII due to the outer skin of this boundary wall is far less pronounced. Hence, we do not observe a sharply increasing value in CaII absorption at ~ 80 pc due to the presence of the boundary wall of the LC. For greater sight-line distances in the general ISM (i.e. $d \gg 100$ pc), the measured CaII equivalent width should be more closely linked to the number of clouds (or cloud envelopes) sampled along a particular sight-line as opposed to the actual distance sampled. Thus we expect to observe a gradual (but variable) increase in CaII absorption equivalent width with distance, as is demonstrated in the increase of $N(\text{CaII})$ with $N(\text{HI})$ by Welsh et al. (1997).

We note that there are only 3 sight-lines within 75 pc with anomalously large values of $W_\lambda(\text{CaII-K})$ in the 20–30 mÅ range. These are the sight-lines towards the stars α Oph ($d = 14$ pc), HD 145570 ($d = 51$ pc), and HD 113852 ($d = 70$ pc). Also, the sight-lines towards HD 5487 ($d = 259$ pc), HD 85504 ($d = 322$ pc) and HD 75855 ($d = 446$ pc) have anomalously low levels of CaII K-line absorption (i.e. $\log N(\text{CaII}) < 10.5 \text{ cm}^{-2}$). These are all high latitude sight-lines that extend through the openings of the low density Local Chimney into the overlying galactic halo.

3.2. The volume density distribution of NaI and CaII

Before progressing to a discussion concerning the creation of 3D density maps of the spatial distribution of both interstellar NaI and CaII gas density, it is informative to firstly investigate the global variation of volume density of both ions as a function of distance sampled. In Fig. 9 we show the plot of NaI volume density, n_{NaI} , (i.e. $N(\text{NaI})/\text{distance}$) versus distance (pc), with upper limit values being plotted as open circles and measured values plotted as filled circles. We note that the lowest values of n_{NaI} are mostly found for distances <200 pc (i.e. the region of the ISM dominated by the effect of the low density LC), although

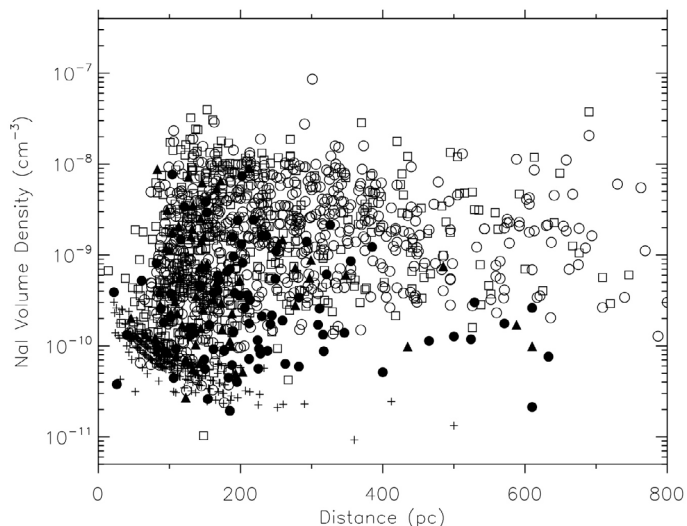


Fig. 9. Plot of the volume density of interstellar NaI absorption for stars with distances <800 pc. Symbols are the same as Fig. 7.

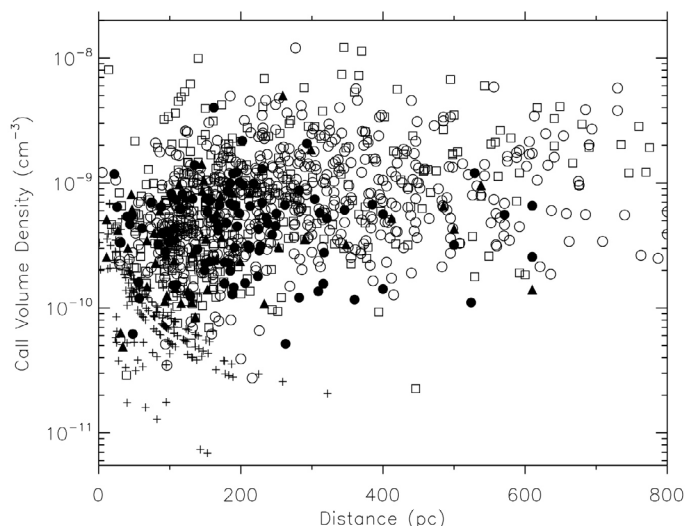


Fig. 10. Plot of the volume density of interstellar CaII absorption for stars with distances <800 pc. Symbols are the same as those in Fig. 7.

there are several sight lines (mostly at high galactic latitudes) with distances up to 600 pc that have similarly small volume density values. In the 110–200 pc distance range there are about a dozen stars with slightly higher than average values of n_{NaI} in the range 10^{-7} – 10^{-8} cm^{-3} . The majority of these stars lie in the longitude range $l = 350^\circ$ – 50° , in the general direction of the galactic center. For sight-lines >300 pc we see a general trend in the data such that values of n_{NaI} in the 10^{-8} to 10^{-10} cm^{-3} range are representative for most distances up to 800 pc. We interpret these latter data points as indicating that the general ISM has a wide range of NaI volume density values, each of which is critically dependent on the number and density of neutral interstellar clouds and interstellar cavities encountered over any given sight-line distance.

In Fig. 10 we plot the volume density of CaII, n_{CaII} , as a function of distance, whose values for sight-lines <100 pc show a complex pattern of behavior. For distances <30 pc we measure both very high and very low values of n_{CaII} , dependent on whether a particular sight-line encounters any of the local fluff clouds. For distances in the 30–100 pc range, although there

are still sight-lines with very low values of $n_{\text{CaII}} < 10^{-10} \text{ cm}^{-3}$, a value of $\sim 5 \times 10^{-10} \text{ cm}^{-3}$ seems fairly representative for most interstellar directions. However, for distances > 100 pc higher values of n_{CaII} are generally encountered in the ISM, such that a volume density of $\sim 10^{-9} \text{ cm}^{-3}$ is typical for most sight-lines with distances up to 800 pc. This would suggest that beyond ~ 100 pc the density distribution of CaII bearing gas is fairly uniform throughout the ISM. This is in accord with the findings of Welsh et al. (1997) and Megier et al. (2005) who both found that the level of interstellar CaII absorption is far better correlated with distance for sight-lines > 100 pc than for NaI absorption.

3.3. Column density inversion maps

Although the plots of equivalent width versus distance can often reveal how absorption accumulates over sight-lines (by revealing gradients in the gas density distribution), the significance of the highest levels of absorption is lost at large distances due to line saturation, and similarly information is lost on absorption with levels less than that of the lowest measurable limit of equivalent width. However the column density inversion method of Vergely et al. (2001) used in Paper I, which derives volume gas densities in 3D space from the integrated sight-line column density values by an iterative inversion process, can reveal masses of gas at any distance provided there are sufficient constraining target measurements.

The inversion algorithm we have presently used to construct the 3D gas density maps is derived from a non linear least-squares approach to the generalised inverse problem (Tarantola & Valette 1982). It differs from a maximum likelihood method in that it allows treatment of under-determined cases by imposing some additional constraints. For the present NaI and CaII data we use “a priori” information on the gas density that follows a Gaussian law with non null spatial autocorrelation. In other words, the computed gas density distribution can be seen as fluctuations around this “a priori” solution. The mathematical specificity is that the solution belongs to the L2 Hilbert functional space, which allows retrieval of the solution everywhere without “a priori” space discretization. For the case of a linear operator linking the unknown parameters (the gas densities) and the data (the measured columns) and an assumed Gaussian fluctuation around the “a priori” value, a solution can be determined directly in one iteration. However this is not the case for our present data (i.e. column densities and distances), since in order to force the gas density ρ to be positive we use a change of variable, namely $\alpha = \log(\rho/\rho_0)$, ρ_0 being a constant. In this case the solution to obtaining the gas density as a function of distance is through an iterative method, as described in Tarantola & Valette (1982) and Vergely et al. (2001).

The inversion method was first applied to opacities in 3D space by Vergely et al. (2001). Here we use the same algorithm, but with the following constraints that are specific to our present set of data: (i) the correlation between the gas density at point X and the density at point X' is of the form $\exp(-|X - X'|^2/\xi^2)$, with a correlation length, ξ , of 20 pc. This distance corresponds to the maximal resolution allowed by the present data set and is roughly the average distance between two target stars. This is an improvement upon our previous inversion of NaI data which used $\xi = 25$ pc, the improvement being allowed by the present larger data set. It implies that details smaller than this characteristic scale will be smoothed out and appear at least 20 pc wide. It also means that the computed volume densities are not the local values, but are mean values in volumes whose size is of the order of 20^3 pc; (ii) the “a priori”

density decreases exponentially with the distance from the galactic plane, with a scale height of 170 pc for Na and 450 pc for CaII. These two values were determined from the data sets themselves by fitting an exponential law (for the density) to the measured columns. (iii) The “a priori” error on the opacity, $\alpha = \log(\rho/\rho_0)$, follows a Gaussian law with a standard deviation $\sigma(\alpha) = 2.5$. This allows high contrasts for the density, i.e. very dense clouds or close to null values. (iv) The errors on the data follow a particular law chosen to minimise the effects of potential outliers within the data set, as originally devised by Vergely et al. (1998), namely:

$$f(c(i) - c_0(i)) = \pi \cdot \sigma(i) \cdot \cos h\left(\frac{(c(i) - c_0(i))}{\sigma(i)}\right) \quad (1)$$

where $f(c(i) - c_0(i))$ is the probability for a specific column density $c(i)$ towards target i to depart from the central data value $c_0(i)$. Developments show that for close values this function tends to a classical Gaussian (a L2 norm), while for values far above or below the central one it tends to vary like $\exp(-(c(i) - c_0(i))/\sigma(i))$, i.e. a L1 norm.

(v) Relative errors on the columns are taken to be 25% for all targets, and those errors are combined with the individual errors on the Hipparcos parallaxes.

Finally, we want to emphasize that within our data set of gas densities there are some locations for which there is no information that can change the volume density from the initial “a priori” value. For these locations the gas density value is kept unchanged. We have included such information in our maps (see below).

The resultant accuracy of the inversion method has been evaluated by Vergely (1998) through extended tests using synthetic cloud distributions. The comparison between these initial synthetic distributions and the resultant inverted densities shows that there are optimal values for both the correlation length (also called the smoothing parameter, x) and the statistical error on the density (i.e. the allowed density fluctuation amplitudes). The correlation length is clearly linked to the average distance between the target stars and the optimal selected value essentially defines the resulting placement accuracy of gas clouds using the inversion method. In our case this distance is of the order of 35 parsecs for the entire target sample, but is less at smaller distances from the Sun. This is because nearby targets are more numerous, and thus more information can be obtained within the first 150 parsecs. Hence we have selected the smaller value of 20 pc for the correlation length in our new maps. However, the standard deviation for density fluctuations must be non-negligible, since we know in advance that there are dense areas and voids between the many groups of dense clouds.

In order for the reader to appreciate the typical accuracy of the inversion method for the placement of interstellar gas clouds, in Fig. 11 we show an example of a fractal distribution of measurements of interstellar reddening in the galactic plane and the corresponding inversion of cloud densities computed for 2500 sight-lines randomly distributed in distance and directions around the galactic plane. These data are taken from Figs. 5.10 and 5.11 of Vergely (1998), with a correlation length of 15 pc and measurement errors being simulated as “noise” in the reddening and distance data. Vergely (1998) found that the broad structures of reddening (which are equivalent to gas clouds) were well located after the inversion, but clouds (or voids) smaller than 10–20 pc were included in broader cloud structures and thus smeared out. Finally, it must also be mentioned that since the inversion method is statistical in nature, it is impossible to

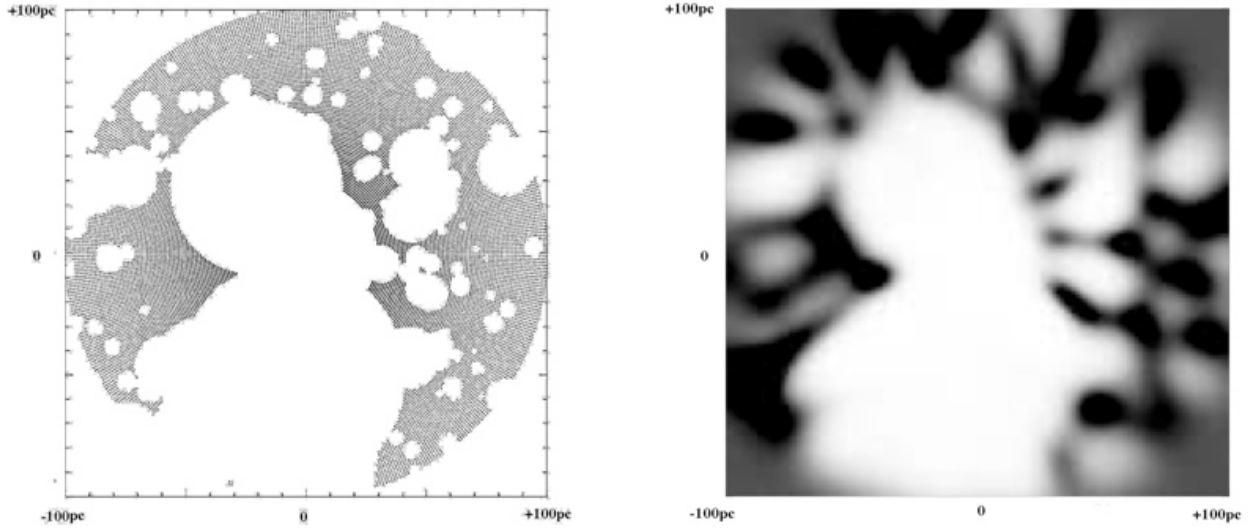


Fig. 11. Comparison of an initial map of the fractal distribution of interstellar reddening in the galactic plane (*left*) and the equivalent map of gas column densities (*right*) derived from the inversion method of Vergely (1998). Most large features are reproduced, whereas small features with sizes < 15 pc are smeared by the inversion method.

prevent some bad restitution for one or more cloud structures. This may happen when the combination of the actual distribution in one particular galactic area and the target sampling in that area are highly non-uniform (i.e. when the region or galactic direction is sparsely sampled).

The end-product of the inversion method, when applied to our present measurements (and associated errors) of column density and distance for each of the sight-lines sampled, is a 3D data cube of NaI (or CaII) gas density as a function of distance and galactic longitude and latitude. Our new NaI volume density data cube has a 60% increase in the number of targets over that of Paper I, and the CaII maps are the first ones of their type ever to be presented. In Paper I the correlation length for the NaI data was ~ 25 pc, whereas the gas distribution shown in our new maps of NaI and CaII can be considered representative at the 20 pc sampling scale. Thus, as mentioned above, small-scale absorption features (i.e. small cloudlets of low density gas) could easily be missed in our final smoothed density maps. For a few cases very high column density values of $\log N(\text{NaI})$ and $\log N(\text{CaII}) \gg 13.5 \text{ cm}^{-2}$ are reported by other authors in Table 1. In some cases it was evident that the absorption profiles had not been fitted with sufficient cloud components and we noted that such very high density values tended to bias and unrealistically distort the 3D mapping program (with associated points of inflection) when low density sight-lines are spatially close to these apparently very dense regions. In order to smooth out this effect, but still retain the presence of the high density regions in our maps, we determined that by generally limiting the maximum values of $\log N(\text{NaI})$ and $\log N(\text{CaII})$ to 13.5 cm^{-2} this distortion effect was minimized in the resultant plots.

Since we have created 3D data cubes for both NaI and CaII gas density out to a distance of 300 pc from the Sun, in principal we can present maps of the spatial density distribution of either ion in any desired galactic projection. However, for brevity, we present maps for the 3 main projections (galactic, meridian and rotational planes) for both NaI and CaII ions. It is envisaged that the entire data-base of absorption measurements, together with the associated 3D gas density cubes for NaI and CaII will be made available to the community on the worldwide web by the end of 2009.

4. NaI absorption within 300 pc

In the following sub-sections we present maps of the 3D distribution of NaI absorption within 300 pc of the Sun, formed from three main galactic projections through the previously described 3D NaI gas density cube. Each of the maps represents the spatial distribution of the volume density of NaI (n_{NaI}) as a function of distance and thus is a 3D visualization of the data previously discussed in Sect. 3.2. Each map shows the regions where very low values of neutral gas density are located (white shading) together with regions where statistically significant amounts of neutral gas have been detected (grey/black shading). Areas with insufficient information to perform an inversion of the columns are indicated by a matrix of dots in the maps. They correspond to areas within which the density is still the “a priori” density. In cases where some information is present but the number of constraints from the target stars makes the location of the cloud, or of the cavity, very imprecise, the inversion process may create “finger-like” extensions that are easily recognisable in the maps. The presence of such features can be interpreted as indications of the existence of a gas cloud along the “finger” direction, but the location of the accumulation of gas is thus uncertain.

Stars used to create each map are shown as triangles with their size being proportional to their distance above (triangle vertex pointing up) or below (vertex pointing down) the galactic plane. Superposed on the maps are contours of iso volume density with values of $\log n_{\text{NaI}} = -9.5, -9.1, -8.5$ and -7.8 cm^{-3} shown respectively in yellow, green, turquoise and blue lines. As an approximate guide, these average values of neutral gas volume density can be converted into hydrogen density values at a particular distance using the relationship given in Ferlet et al. (1985). Finally, we further remind the reader not to over-interpret every absorption feature that appears in these maps due to the reasons listed previously.

4.1. NaI: a view from above the galactic plane

The greatest number of sources (i.e. early-type stars) sampled by this survey lie close to the galactic plane and hence the gas density maps derived for both NaI and CaII for this particular

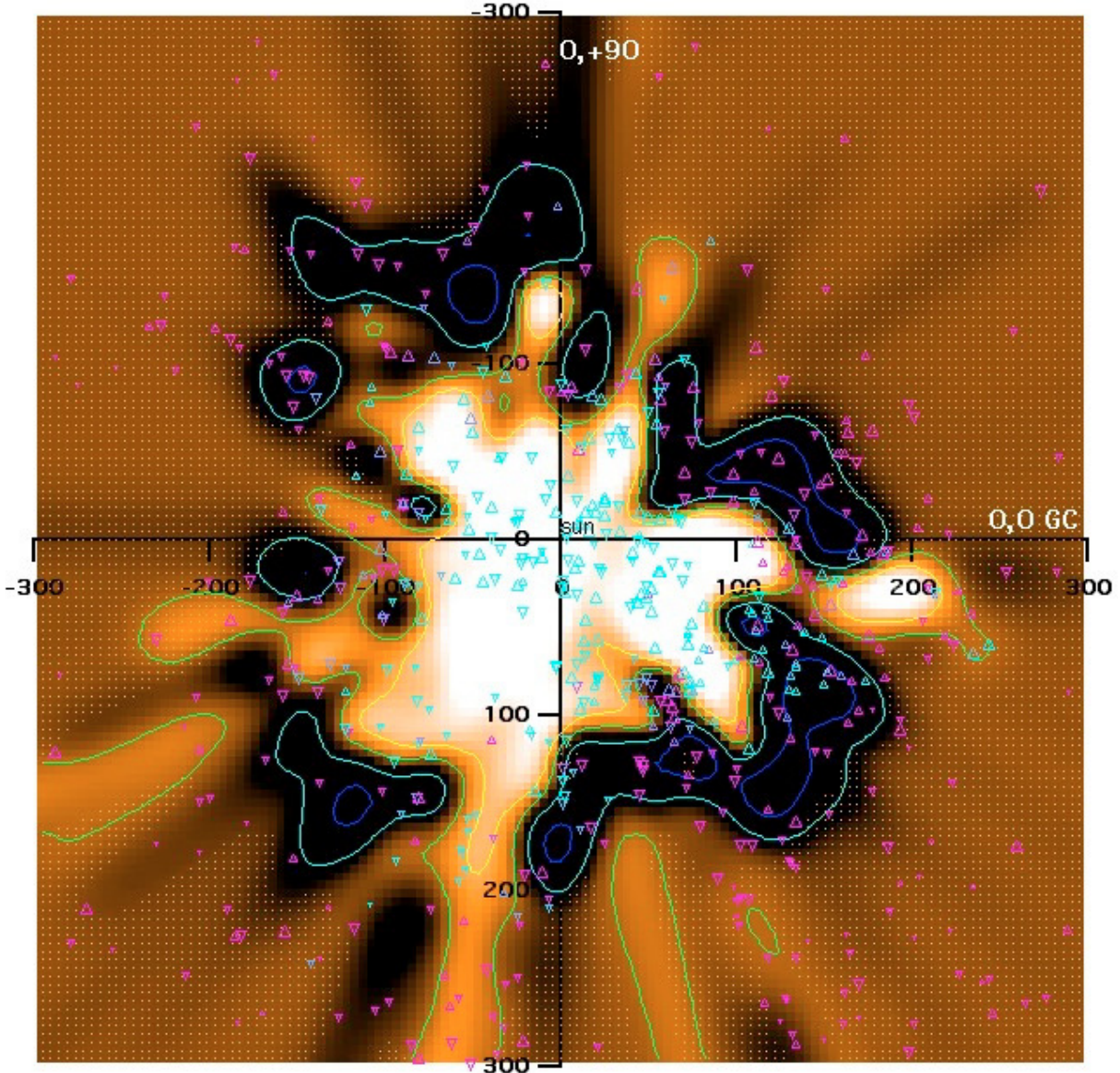


Fig. 12. Plot of 3D spatial distribution of interstellar NaI absorption within 300 pc of the Sun as viewed in the galactic plane projection. Triangles represent the sight-line positions of stars used to produce the map, with the size of the triangle being proportional to the derived NaI column density. Stars plotted with vertex upwards are located above the galactic plane, vertex down are below the plane. White to dark shading represents low to high values of the NaI volume density (n_{NaI}). The corresponding iso-contours (yellow, green, turquoise and blue) for $\log n_{\text{NaI}} = -9.5$, -9.1 , -8.5 and -7.8 cm^{-3} are also shown. Regions with a matrix of dots represent areas of uncertain neutral gas density measurement.

galactic projection are the most accurate. In Fig. 12 we show the spatial distribution of NaI density to 300 pc which clearly reveals a large and highly irregularly shaped volume of space surrounding the Sun to a distance of ~ 80 pc in most directions that is devoid of dense condensations of cold and neutral gas clouds. This region, of course, can be identified as the Local Cavity (LC). We note that the LC is more elongated in galactic quadrants 3 and 4 compared with the other two quadrants, with quadrant 1 having the smallest volume of low-density neutral gas. Our new map also reveals for the first time that the LC (in the galactic plane) can essentially be considered as two rarefied “sub-cavities” that abut each other along a thin interstellar gas filament of low column density ($(\log N(\text{NaI}) \sim 10.4 \text{ cm}^{-2})$ at a distance of ~ 15 pc in the direction of $l \sim 345^\circ$. One of these “sub-cavities” is mostly contained within galactic quadrants 2 and 3 (and to a far lesser extent within quadrant 1), with the majority of the other low

density “sub-cavity” mostly being contained within quadrant 4. The appearance of smaller “cell-like” cavity structures bounded by thin gas filaments is also hinted at in the equivalent maps of CaII absorption and these will be discussed further in Sect. 5.1.

The relatively dense neutral gas wall that surrounds the LC in the galactic plane has a typical depth of 50–80 pc in most directions, but it is quite evident from the map that the LC void is *not* fully enclosed by a continuous boundary of cold and neutral gas. Instead, the LC can be best described as being “porous” in the sense that it appears to be linked to several adjacent interstellar cavities through narrow gaps in the surrounding neutral gas wall. These adjacent interstellar cavities include the Loop I superbubble, the β CMA interstellar tunnel and the Pleiades bubble, all of which were revealed in the preliminary maps presented in Paper I. Our new map now reveals that the tunnel of low interstellar gas density towards the direction of

the star β CMa ($l = 226^\circ$) is bifurcated at a distance of ~ 160 pc, which is also the distance to β CMa itself. The tunnel's most pronounced region of low neutral density extends to at least 250 pc in the direction of $l \sim 260^\circ$, which provides a pathway to the GSH 238+00+09 supershell which may have been created by the star cluster Collinder 121 (Heiles 1998). The pathway to the Loop I region ($l \sim 345^\circ$) is now revealed to be far narrower than that originally shown in Paper I, with only one low density passageway leading towards the Sco-Cen OB association. The present map shows this narrow entrance to consist of several fragmented clouds located over the distance range 90–120 pc, in agreement with previous UV observations of this region by Welsh & Lallemand (2005). Our new map shows three other regions of low neutral gas density (interstellar bubbles?) that exist beyond the neutral boundary to the LC at distances >200 pc. These are located in the directions of $l = 190^\circ$ (Taurus), 210° (Orion/Eridanus) and 285° (Carina).

Figure 12 also reveals a previously unknown gap in the neutral boundary to the LC in the galactic plane that lies between $l = 70^\circ$ to 80° . This low density extension of the LC lies in the direction of Cygnus and may be linked to part of the Loop II SNR which lies at a distance of ~ 110 pc (Berkhuijsen 1973). We note that in the direction of this newly discovered gap in the LC wall there is a large patch of emission revealed in both the 3/4 keV and 1/4 keV maps of the SXR (Snowden et al. 1997). The presence of such (low neutral gas density) gaps and openings in the wall of the LC should have a profound effect on the potential observability of more distant sources of soft X-ray diffuse emission. Although this effect is most pronounced when viewing the halo through the openings of the Local Chimney at high galactic latitudes (see Sect. 4.2), the gaps may also provide a low absorption path for emission from soft X-rays generated in nearby hot superbubbles. For example it is well-known that there is a dipole effect in the distribution of the soft X-ray background emission, with the emission being warmer, of greater intensity and with a larger spatial coverage in directions towards the galactic center than along sight-lines towards the galactic anti-center at mid-plane latitudes (Snowden et al. 2000). This effect may now be explained through inspection of Fig. 12 which shows that the local void is linked to the Loop I superbubble (which is a known source of million degree soft X-ray emission) through a gap in the surrounding boundary wall in the direction of the galactic center.

The closest accumulations of neutral gas in the galactic plane (with $\log N(\text{NaI}) \sim 10.8 \text{ cm}^{-2}$) are located in the directions of (i) $l \sim 85^\circ$ at a distance of ~ 38 pc towards the star HD 184006; (ii) in the general direction of the galactic center at a distance of ~ 50 pc (towards HD 159170); and (iii) towards several stars with distances in the 60–80 pc distance range in the direction of $l \sim 285^\circ$. All 3 of these low neutral density gas clouds are extensions of the surrounding denser neutral wall that protrude into the central regions of the LC. They appear to form the filamentary gas boundaries to the inner cell structures whose possible presence within the larger LC was alluded to previously.

In addition, in the direction of $l \sim 195^\circ$ at a distance of ~ 95 pc we detect another small, more dense gas cloud. The presence of two small gaps in the neutral wall to the LC in this general direction at $l = 165^\circ$ and $l = 190^\circ$ suggest that the isolated dense cloud is most probably part of the broken boundary wall to the LC. Finally, we note that although our sampling of targets with distances in the 200–400 pc range is far from complete (as indicated by regions of small dots in the map), there do appear to be galactic directions in the galactic plane in which the neutral gas density does not increase with the distance

sampled. For example, in the direction of $l = 315^\circ$ we have an appreciable number of targets sampled with distances >200 pc which show no additional NaI absorption beyond that distance. This suggests that there may be other large regions of low neutral gas density (i.e. superbubbles) that remain to be revealed by future more extensive absorption measurements in the interstellar region between 200 and 400 pc from the Sun.

4.2. NaI absorption viewed in the meridian plane

In Fig. 13 we show the spatial distribution of NaI absorption to 300 pc as projected in the meridian plane with the galaxy essentially being viewed in a side-on manner. The plotting symbols are the same as those for Fig. 12. The cold and dense NaI absorption associated with gas in the galactic plane can be seen as a ~ 200 pc (vertically) thick gaseous bar that stretches from left to right across Fig. 13. The low neutral density void in the central region of this plot is the LC, which in this projection can be identified with the open-ended Local Chimney that is tilted at an angle of $\sim 35^\circ$ from vertical. This new plot confirms the recent studies of Crawford et al. (2002) and Welsh et al. (2004), in which no continuous neutral boundary to the LC can be found at high latitudes in either galactic hemisphere. This map also confirms the general lack of neutral gas for sight-lines that extend to at least ~ 175 pc into the inner halo regions. We also note that the rarefied Local Chimney region fragments into finger-like extensions that reach into the inner halo in both hemispheres. Filaments of neutral HI gas have been widely observed in the general ISM and their appearance within the local ISM suggests that they may be linked to the origin of the LC in which an explosive event may have “cleared out” any neutral gas that may have once resided close to the Sun and ejected it into the overlying galactic halo.

Figure 13 shows four major condensations of cold neutral gas lying *within* the confines of the LC in this galactic projection. They appear to lie along a fragmented bar of dense gas that lies at an angle of $\sim 45^\circ$ to the galactic plane that stretches from 200 pc below to 30 pc above the plane. The nearest of these clouds lies at a distance of ~ 50 pc at a galactic latitude of $b \sim 30^\circ$ towards HD 145570 and it is an extension of the more distant dense wall to the LC in that direction. The three remaining neutral clouds appear as a string of gaseous “blobs” in the direction of ($l \sim 165^\circ$, $b \sim -75^\circ$) at distances of 60 pc (towards HD 9672), 110 pc and 180 pc. The cloud of cold neutral gas at 110 pc can be associated with the translucent molecular cloud G192-67 (Grant & Burrows 1999). This string of 3 nearby clouds would be an ideal candidate for future soft X-ray shadow observations that potentially could resolve the outstanding issue of the degree of pervasiveness of the purported million degree gas that may be present within the Local Cavity (Welsh & Shelton 2009). Finally, Fig. 13 also shows a thin and elongated cloud of neutral gas at a distance of ~ 200 pc in the galactic direction of ($l \sim 335^\circ$, $b \sim -30^\circ$), whose existence is revealed for the first time.

4.3. NaI absorption viewed in the rotational plane

Figure 14 is perhaps the most changed of all three neutral density maps when compared to the previous presentations of Paper I, due to the small number of target stars available along this plane in the previous work. The low neutral density rarefied LC region extends to ~ 60 pc in most directions, and the surrounding fragmented wall of much denser neutral gas is generally not encountered until a distance of ~ 100 pc. As also revealed in the meridian projection of Fig. 13, there is no continuous neutral boundary

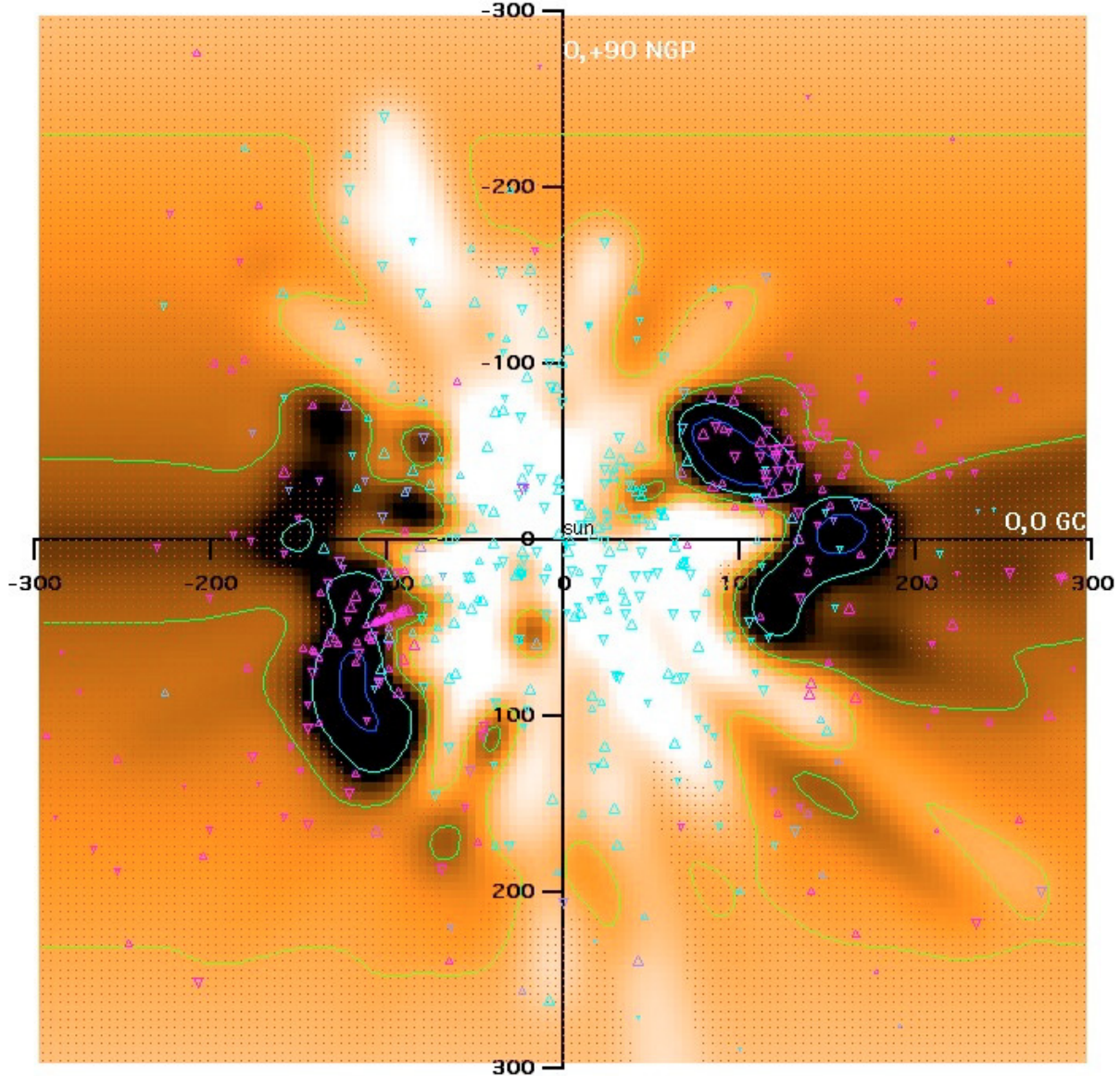


Fig. 13. Plot of 3D spatial distribution of interstellar NaI absorption within 300 pc of the Sun as viewed in the meridian plane projection. Plotting symbols are the same as those given for Fig. 11.

to the LC at high latitudes in both galactic hemispheres. In the rotational projection we see that the Local Chimney has only one major narrow opening towards the north galactic pole (tilted at $b \sim +75^\circ$), whereas the opening into the galactic halo in the southern hemisphere is of far larger dimensions. Figure 14 also shows narrow extensions of the rarefied inner LC to distances as far as ~ 200 pc in several directions. Their finger-like shape means their distances are not well constrained, but it is interesting to try and relate them to known distant features. The most prominent of these cavity extensions are seen towards the southern galactic pole and also towards $l \sim 250^\circ$ close to the galactic plane. The latter feature is the pathway to the GSH 238+00+09 supershell discussed previously in Sect. 4.1.

Figure 14 suggests that there are no large accumulations of neutral gas contained within the confines of the rarefied LC in this projection. The nearest edge of a NaI cloud is at a distance of ~ 40 pc in the direction of $l \sim 90^\circ$ near to the galactic plane (towards the stars HD 184006 and HD 186882). This cloud appears to be an extension of the denser neutral wall to the LC in this galactic direction. We further note the presence of two

denser NaI clouds at distances of ~ 85 pc and 110 pc at galactic latitude $b \sim 75^\circ$. Both clouds are also probably fragments of the surrounding disk gas that may have been disrupted by the expansion of the original Local Bubble into the overlying less dense galactic halo.

One particularly interesting feature shown in this map is the circular region of low neutral gas density at a distance of ~ 140 pc that lies 25° above the galactic plane in the general direction of ($l \sim 90^\circ$). The low level of absorption along this sight-line was first reported by Lilienthal et al. (1991) and we now confirm the presence of a large interstellar cavity with similar dimensions to that of the Loop I superbubble feature.

For completeness we note that Meyer et al. (2006) have reported the detection of a very cold ($T \sim 20$ K) neutral NaI cloud located at a distance of ~ 45 – 55 pc in the direction ($l \sim 230^\circ$, $b \sim +45^\circ$). Unfortunately the galactic position of this cloud is such that it does not appear in any of the 3 galactic projections we have currently presented. However, this is an important detection since the cloud's presence within the Local Cavity has been posed as a challenge to current theories concerning the

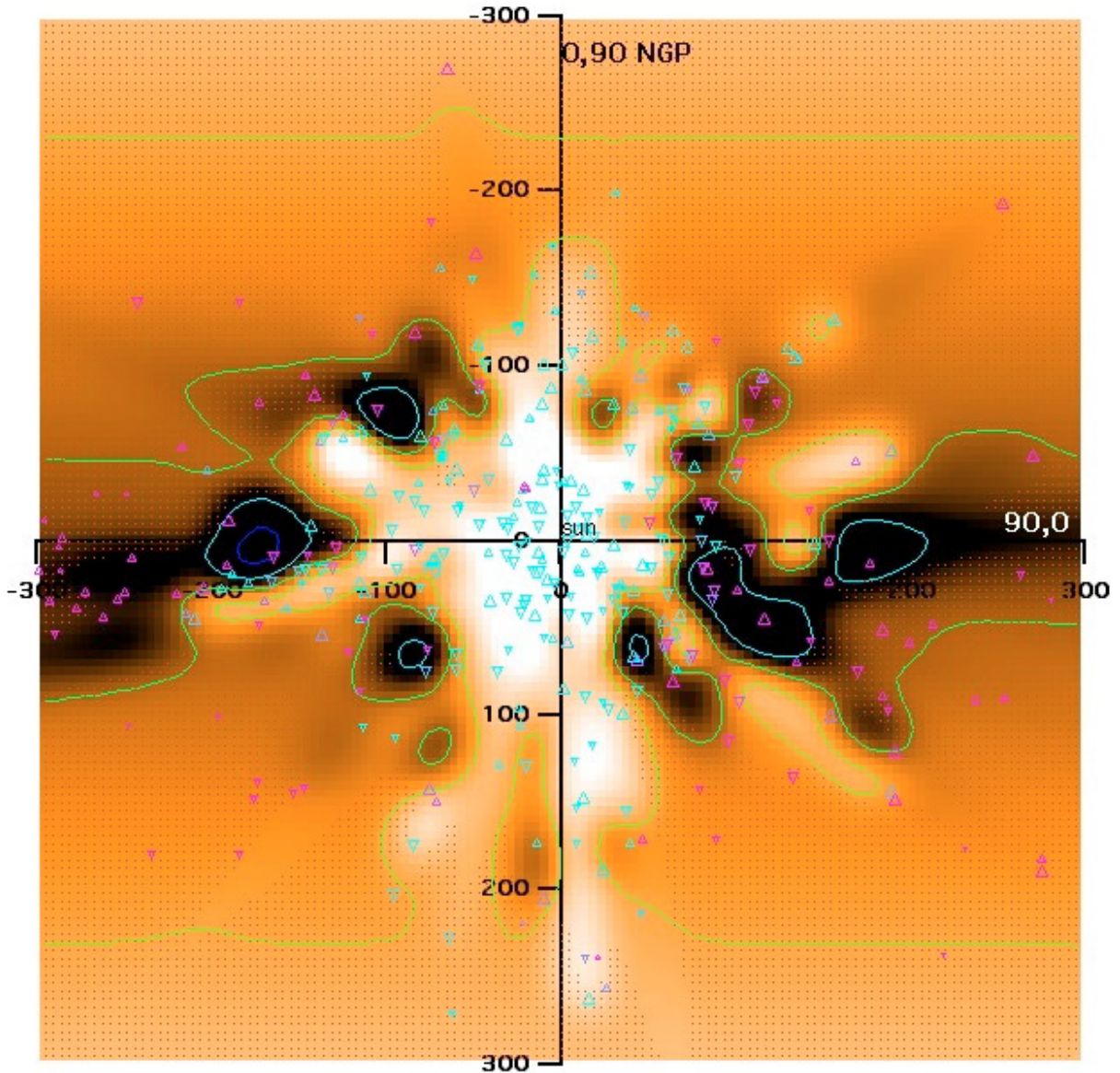


Fig. 14. Plot of 3D spatial distribution of interstellar NaI absorption within 300 pc of the Sun as viewed in the rotational plane projection. Plotting symbols are the same as those given for Fig. 11.

survival of cold gas clouds that may be immersed in a purportedly hot (million K) surrounding plasma.

5. CaII absorption within 300 pc

In the following sub-sections we now present three maps of the spatial distribution of CaII absorption within 300 pc of the Sun, formed from a 3D CaII volume density cube derived in a similar manner to that described for the NaI data. The new maps, derived with a correlation length of 20 pc, are shown in Figs. 15–17 and have the same plotting symbols as those presented for NaI, except that the CaII volume density iso-contours (yellow, green, turquoise and blue) correspond to values of $\log n_{\text{CaII}} = -9.9, -9.5, -8.9$ and -8.2 cm^{-3} .

5.1. CaII: a view from above the galactic plane

As was the case for the NaI data, this map has the largest number of sight-line measurements of CaII and thus is the most accurate of the 3 different galactic projections all presented here for

the first time. The overall appearance of Fig. 15 shares a gross similarity with the equivalent plot for NaI absorption in that it reveals a central region of mainly low density CaII gas that is surrounded by a highly fragmented wall of denser partially ionized gas clouds. However, on closer examination of Fig. 15 we see that (in common with the NaI data) the LC is not one large volume of rarefied low neutral density gas, but in fact it can be better described as a collection of several smaller low density cavities that are each surrounded by thin gas filaments of slightly higher density neutral and/or partially ionized material. Although some of these filamentary structures may be artifacts caused by uncertainties in the inversion mapping method when only a few target measurements are present along a given sight-line, this is not the case for all of the diffuse gas filaments that appear to be present in Fig. 15. Clearly, although more measurements will be required to confirm the reality of a collection of cell-like cavity structures that may be present within the LC, such a scenario would have some intriguing astrophysical ramifications. For example, how could such small interstellar cell-like cavities form within the Local Cavity? One possibility is

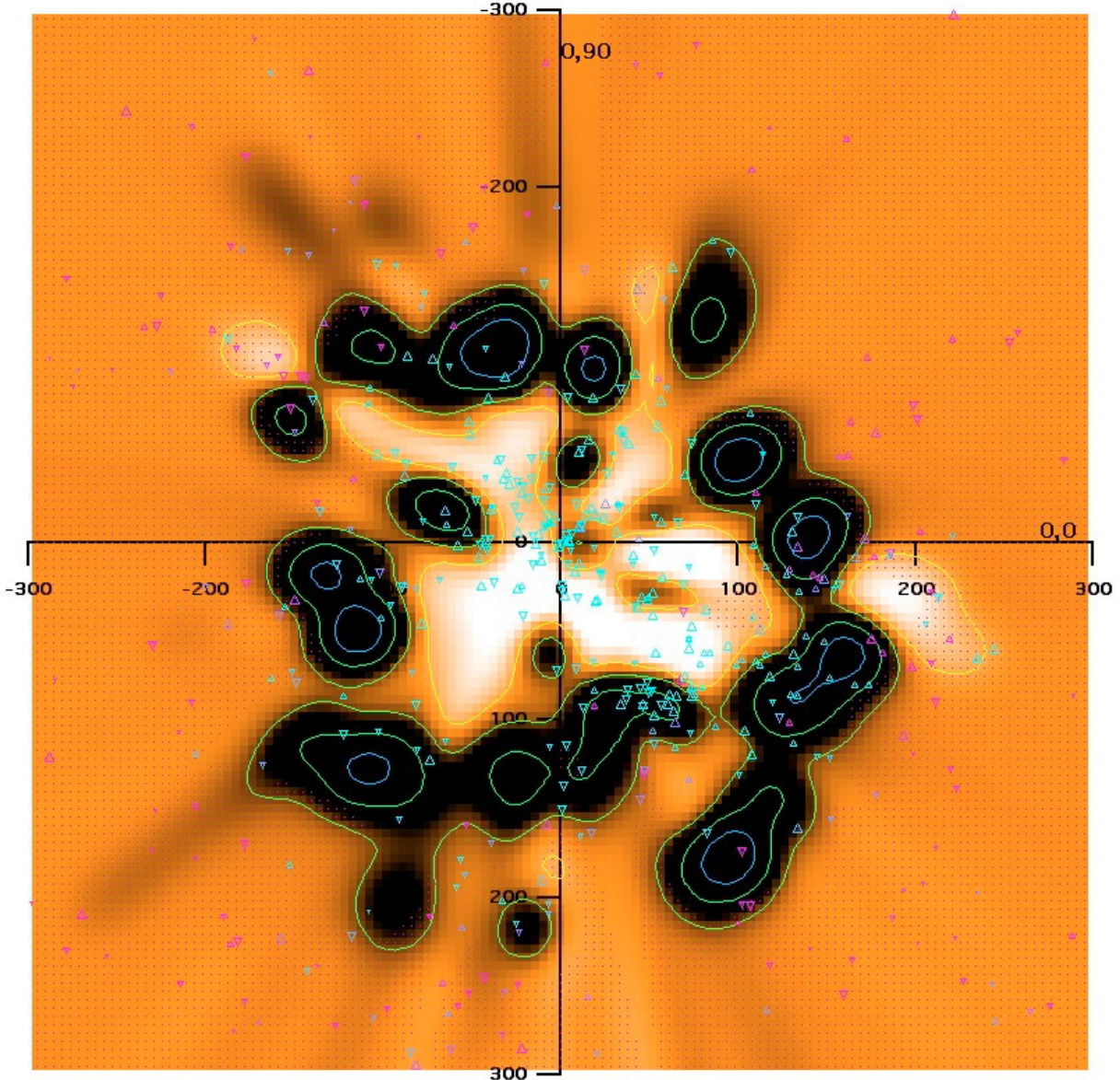


Fig. 15. Plot of 3D spatial distribution of interstellar CaII absorption within 300 pc of the Sun as viewed in the galactic plane projection. Plotting symbols are the same as Fig. 11, except that the volume density iso-contours (yellow, green, turquoise and blue) correspond to $\log n_{\text{CaII}} = -9.9, -9.5, -8.9$ and -8.2 cm^{-3} .

that each of the rarefied sub-cavities could be a small ionized stellar HII region (with a neutral/partially ionized filamentary gas envelope) formed by the stellar wind action of nearby early B-type stars (and to a lesser extent by local hot white dwarfs). We note that there are at least 11 stars of spectral type earlier than B3V located within 100 pc of the Sun whose combined stellar UV flux may be responsible for photo-ionization of the surrounding low density medium. This scenario would provide a natural explanation for the observed ionization state of the local interstellar medium as measured over many local sight-lines by Lehner et al. (2003). We note that previous estimates of the ionization sources of the local ISM have assumed the presence of a hot million degree gas in addition to photoionization from the early-type star ϵ CMa in order to explain the physical state of the local interstellar cloud (Slavin & Frisch 2008). Unfortunately a detailed calculation and comparison of the local ionization field is beyond the scope of this present work, and we urge theorists in this field to test whether the picture of a Local Cavity with no million degree gas (Welsh & Shelton 2009), but instead

containing a collection of small ionized HII region cavities can reproduce the UV absorption line strengths and velocity structure widely observed along local sight-lines by Lehner et al. (2003) and Welsh & Lallement (2005).

In contrast with the equivalent absorption map of NaI, the central region of the LC has at least six condensations of appreciable CaII absorption (i.e. clouds of partially ionized gas) lying within 80 pc of the Sun. The nearest region of CaII absorption is the complex of local interstellar clouds that extend to ~ 15 pc mostly in directions contained within galactic quadrants 1 and 4. Redfield & Linsky (2008), using both ground-based and UV absorption observations recorded towards nearby stars, have presented more detailed maps of each of the several clouds that contribute to this local cloud complex and argue that the Sun is located in a transition zone between two of these clouds. Our results are in quantitative agreement with their results, with the majority of this local CaII absorption being attributed to the presence of the local interstellar cloud, the G-cloud and the Blue cloud (Lallement et al. 1995; Redfield & Linsky 2008).

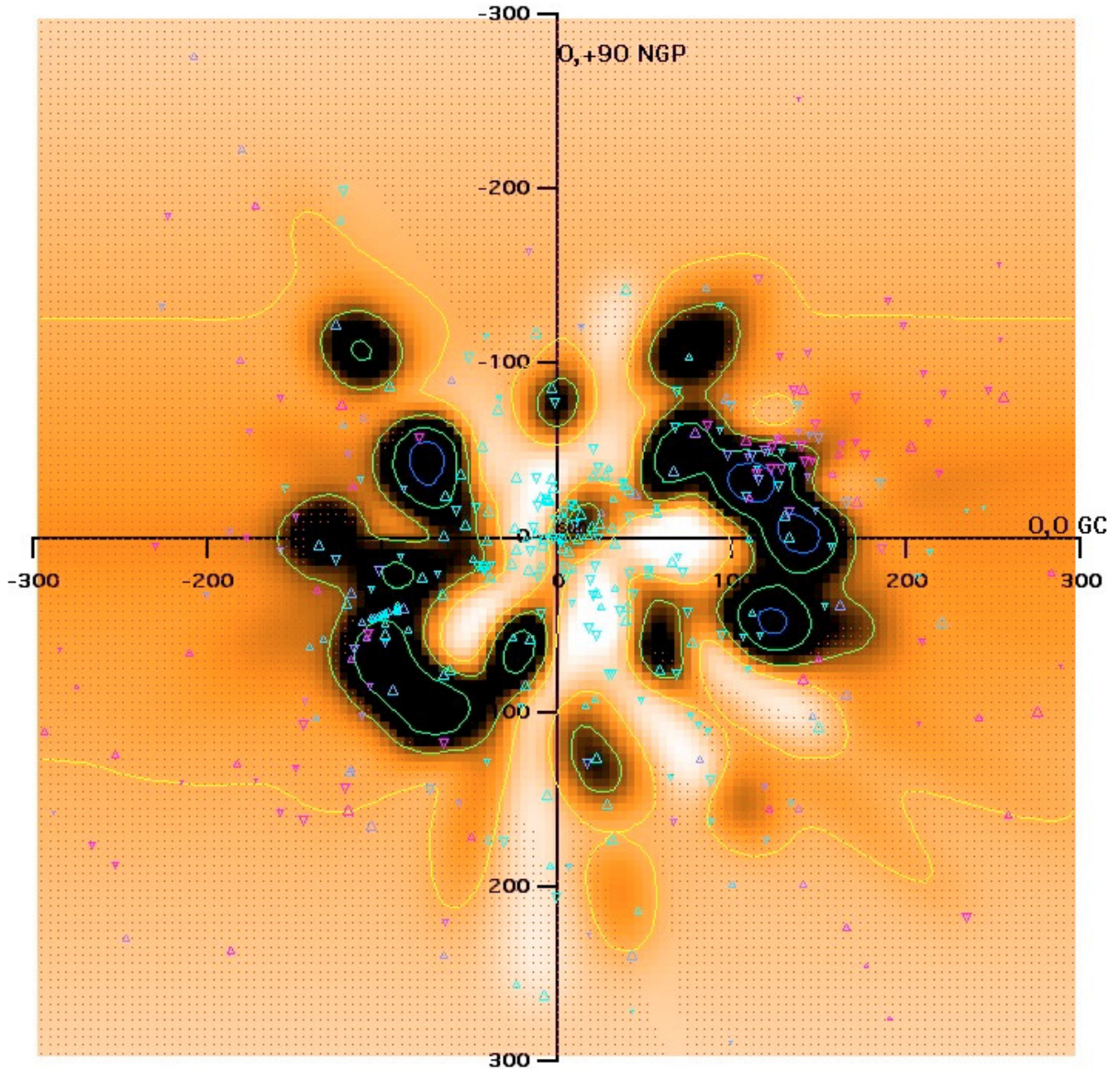


Fig. 16. Plot of 3D spatial distribution of interstellar CaII absorption within 300 pc of the Sun as viewed in the meridian plane projection. Plotting symbols are the same as Fig. 14.

The second nearest region of appreciable CaII absorption is located at a distance of ~ 50 pc in the general direction of ($l \sim 80^\circ$) towards the stars HD 186882 and HD 193369. This feature is also seen in the corresponding NaI absorption map as a very low neutral density finger-like gas cloud that looks like an extension of a larger and denser interstellar cloud located at ~ 100 pc in the same galactic direction. The third nearest region of CaII absorption is located at ~ 55 pc in the direction of ($l \sim 325^\circ$) towards the stars HD 134481, HD 134482 and HD 141194. It has no apparent NaI counterpart. The fourth nearest region of CaII absorption is located at a distance of ~ 60 pc in the direction of ($l \sim 20^\circ$) and this may either be an extension of the local interstellar cloud complex in this direction or a protrusion from the surrounding wall to the LC. Finally, there are two regions of appreciable CaII absorption located at about 70 pc towards $l \sim 265^\circ$ and $l \sim 170^\circ$. While the former cloud has a slightly more distant NaI counterpart, none is clearly seen for the second regions. This gas may be strongly photo-ionized, as is the case for more distant gas seen in this direction (see next paragraph).

Figure 15 shows that the dense CaII (and NaI) cloud structures that surround the LC are accompanied by many narrow pathways (tunnels) of lower CaII gas density that extend into surrounding interstellar regions. Many of the dense regions of NaI absorption that surround the LC close to the galactic plane (as shown in Fig. 11) are also seen as high density CaII-bearing clouds at the same physical locations. In addition, most of the interstellar tunnels revealed by the paucity of NaI absorption in Fig. 12 (and discussed in Sect. 4.1) are also observed as low density regions in the CaII absorption map of Fig. 15. The major exception to this is the low neutral density Cma tunnel ($l = 226^\circ$) that is so prominent in the NaI maps. Figure 15 reveals this direction to possess a high level of CaII gas density, which is to be expected if this tunnel of interstellar gas is photo-ionized by the two early-type stars of ϵ and β Cma (Vallerga 1998). We also note that the narrow interstellar tunnel of low neutral gas density leading into the more distant cavity at ($l \sim 345^\circ$) is significantly more obscured in the CaII maps. In contrast, the region lying beyond 150 pc in this direction is devoid of both neutral and

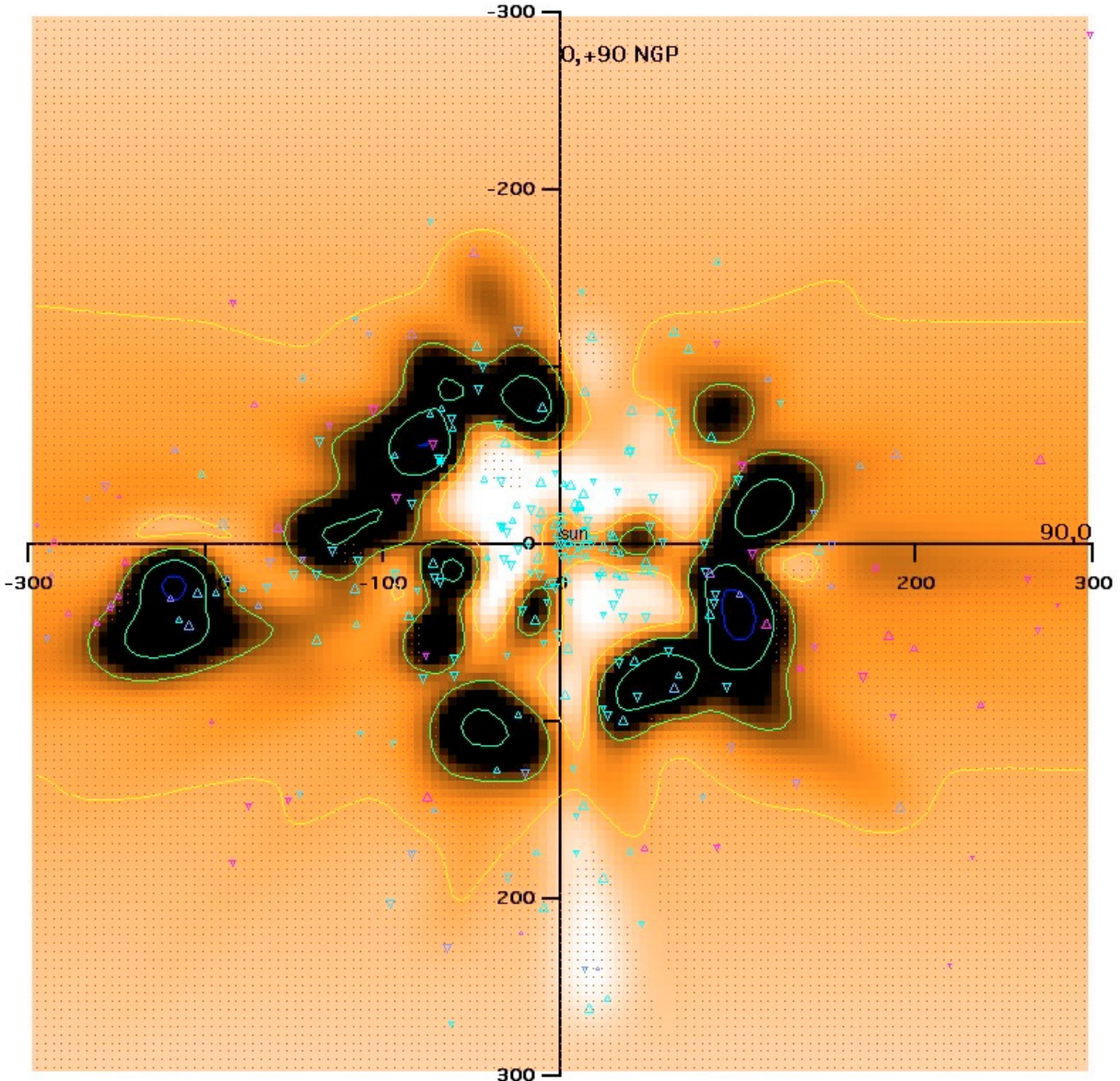


Fig. 17. Plot of 3D spatial distribution of interstellar CaII absorption within 300 pc of the Sun as viewed in the rotational plane projection. Plotting symbols are the same as Fig. 14.

partially ionized gas, as one might expect if the cavity (which we associated with the Loop I superbubble) is hot and highly ionized.

The main conclusion from Fig. 15 is that there are a significant number of partially ionized diffuse gas clouds that are present within the LC. Their ubiquity, current state of ionization and gas temperature have yet to be fully accounted by any model of the local ISM (Slavin & Frisch 2008; Vallerga 1998; Bruhweiler & Cheng 1988), and thus we urge a re-assessment of some of these models in the light of the recent findings of the lack of a local million degree gas and the possible existence of cell-like cavity structures within the LC.

5.2. CaII absorption viewed in the meridian plane

In Fig. 16 we show the spatial distribution of CaII absorption within 300 pc as projected in the galactic meridian plane. The central region of low CaII absorption density essentially mimics the Local Chimney feature shown in Fig. 13 for NaI absorption,

but the corresponding CaII Chimney has a narrower diameter of ~ 100 pc and reveals several small cell-like structures within the rarefied central region. The LC (when viewed in CaII) is also seen to be open-ended towards both high and low galactic latitudes, with a larger (fragmented) opening towards the southern hemisphere, in concert with the corresponding map of NaI neutral gas absorption. The central low density volume of the LC is surrounded in the galactic plane by dense partially ionized CaII gas clouds mostly located within the galactic disk. Many of these clouds are also seen in the equivalent NaI absorption map of Fig. 13. However, we note that the narrowing of the Chimney in Fig. 16 is mainly due to the presence of dense CaII clouds located in galactic quadrants 2 and 3 whose full extent are not traced by NaI absorption. For example, the string of 3 gaseous NaI “blobs” seen in the direction of ($l \sim 165^\circ$, $b \sim -75^\circ$) in Fig. 12 have a CaII counterpart that has the appearance of a large hook-like cloud that comes as close as ~ 40 pc to the Sun.

There are 3 major condensations of partially ionized CaII gas lying within 100 pc of the Sun in this projection. The nearest of

these is the local cloud complex ($d < 15$ pc) that partially surrounds the Sun and has been discussed in the previous section. We note that, as suggested by the galactic plane projection map, this cloud appears to be physically linked to the wall of denser gas that surrounds the LC region in the direction of the galactic center. The second closest cloud of high CaII gas density lies at a distance of ~ 70 pc in the direction of the north galactic pole. This cloud has no apparent NaI counterpart. The third closest dense cloud of CaII is located at a distance of ~ 85 pc with a galactic latitude, $b \sim -50^\circ$, and again it has no apparent counterpart in the equivalent NaI absorption map.

In the direction of the south galactic pole we find a region of high CaII absorption at a distance of ~ 130 pc, whose position is coincident with that of a finger-like extension of low density neutral gas seen in Fig. 13. On the other hand, the large circular CaII cloud in the general direction of $l \sim 180^\circ$ and distance ~ 150 pc with a galactic latitude of $b \sim +45^\circ$ has no NaI counterpart. Due to the lack of suitable targets with distances > 200 pc at high galactic latitudes, we are unable to trace the distribution of partially ionized gas further into the lower galactic halo. Clearly, additional observations of fainter and more distant early-type stars will be required in order to accomplish this task.

5.3. CaII absorption viewed in the rotational plane

Figure 17 shows the spatial distribution of CaII absorption within 300 pc in the galactic rotational plane projection. We observe a large circular volume of very low CaII absorption density that surrounds the Sun to a distance of ~ 80 pc in most directions. This low density cavity has an 80 pc wide opening into the overlying galactic halo at high positive latitudes, but there is only a narrow tunnel of low CaII gas density that leads into the inner halo towards the southern galactic pole. Within the central low density region there are only two clouds of high density CaII absorption, both of which seem to be physically part of a bar of partially ionized gas that includes the local interstellar cloud (within which the Sun is partially immersed). One of the high density regions of partially ionized gas is located at ~ 50 pc in the galactic plane in the direction of $l \sim 90^\circ$, and can be identified with the spatially coincident gas cloud detected in NaI and discussed in Sect. 4.3. The other local high density CaII cloud is in the general direction of $l \sim 270^\circ$ at a distance of ~ 35 pc, located just below the Sun in Fig. 17. This cloud complex can be identified with absorption due to both the interstellar G-cloud and Auriga cloud as listed by Redfield & Linsky (2008). We also note that the bar of CaII gas within the LC seems to be linked to the surrounding boundary wall (at least in the direction of $l \sim 90^\circ$). Its physical shape and dimensions are suggestive of a cell-like structure, in agreement with the local web of low-density interstellar sub-cavities discussed in Sect. 5.1.

The fragmented wall of high CaII gas density that mostly surrounds the central LC region is generally matched with spatially coincident regions of high NaI neutral gas density. However, this one-to-one matching is not always observed. For example, the tunnel of low neutral density gas that opens into the galactic halo towards the north galactic pole shown in Fig. 14 is seen to be spatially coincident with a high density region of CaII absorption. Similarly, the large high density CaII cloud at 110 pc seen towards the south galactic pole is matched by a similarly large region of very low NaI gas density. This pattern of NaI and CaII absorption behavior is reflected in the derived NaI/CaII column density ratio, whose major variations within 300 pc are discussed in the following section.

6. Variation of the NaI/CaII ratio

The column density ratio of $N(\text{NaI})/N(\text{CaII})$ is a well-known diagnostic of the physical conditions in the diffuse interstellar gas, since Ca is more sensitive than Na to the balance between adsorption on, and desorption from, interstellar grains (Barlow 1978). In cold ($T \sim 30$ K) and dense gas clouds, in which most of the gas-phase Ca is depleted onto grains, the NaI/CaII ratio is > 100 . However, in the warmer ($T \sim 1000$ K) and lower density ISM where much of the Ca remains in the gas phase, ratios of < 1.0 are commonly found (Hobbs 1975; Centurion & Vladilo 1991; Bertin et al. 1993). For sight-line distances ≤ 30 pc the NaI/CaII column density ratio for the warm ($T \sim 7000$ K) local interstellar gas clouds is ~ 0.2 (Bertin et al. 1993). Equilibrium equations show that at 7000 K the NaI/CaII ratio is independent of electron density and as a consequence this ratio becomes a tracer of the level of calcium elemental depletion for the local gas.

Beyond the LC and in the general ISM the NaI/CaII ratio is thought to be a function of gas cloud velocity, such that at velocities ≥ 30 km s $^{-1}$ interstellar dust grains may be destroyed by shocks and the Ca is liberated into the gas phase (Routly & Spitzer 1952; Siluk & Silk 1974). Thus, as has been argued by Crawford et al. (2002), a low value of the NaI/CaII ratio could therefore be due to either the presence of warm and partially ionized gas and/or the presence of interstellar shocks. Since we do not expect, nor have observed, interstellar gas with velocities ≥ 30 km s $^{-1}$ in the local ISM then for distances ≤ 100 pc any variation in the observed NaI/CaII ratio is most probably due to temperature/ionization effects. From our sample of stars that possess measured values of both NaI and CaII column densities we see that there is a range in NaI/CaII ratio values of 0.03 to 100, with the vast majority of sight-lines having ratio values < 5.0 . Since the column density values listed in Table 1 are total integrated values measured over the entire length of each sight-line, the derived NaI/CaII ratio value is a sight-line average value. Thus, variations in the ratio for low column density cloud components that may be present along a particular sight-line will be masked by the column density contribution from any high column density (cold and dense) regions. One example of this is shown in Fig. 2 for HD 30112, whose total NaI/CaII column density ratio is 2.1 whereas the $V \sim 5$ km s $^{-1}$ cloud component has a ratio of only 1.15. Thus, we defer a detailed study of the spatial variation of the NaI/CaII ratio in the local ISM to the forthcoming paper by Lallement et al. (2010) that will focus on the cloud component velocity structure of these sight-lines.

In Fig. 18 we show plots of the column density ratio of NaI/CaII as a function of distance to 400 pc for sight-lines with latitudes near the galactic plane ($b \pm 20^\circ$) and split by longitude into 4 galactic quadrants. We see that for distances < 80 pc the majority of measured values of the NaI/CaII ratio lie in the 0.1 to 1.0 range, in general agreement with the low value for this ratio found by Bertin et al. (1993) for stars within the Local Cavity. For more distant sight-lines the NaI/CaII is more variable, but in most directions the ratio value falls in the range 0.5 to 20. This is in agreement with previous work on the NaI/CaII ratio in the general ISM by Welty et al. (1996).

The highest values of the NaI/CaII ratio near the galactic plane are found in quadrant 2 in the direction of $l \sim 150^\circ$ towards the Taurus dark clouds (i.e. along sight-lines towards HD 23180 (55.0), HD 23552 (72.4), HD 24398 (85.1) and HD 25642 (102.3)). There appears to be qualitative agreement in the distribution of the NaI/CaII with distance in all 4 galactic quadrants, with a smaller range of ratio values (typically 0.1 to 5) present

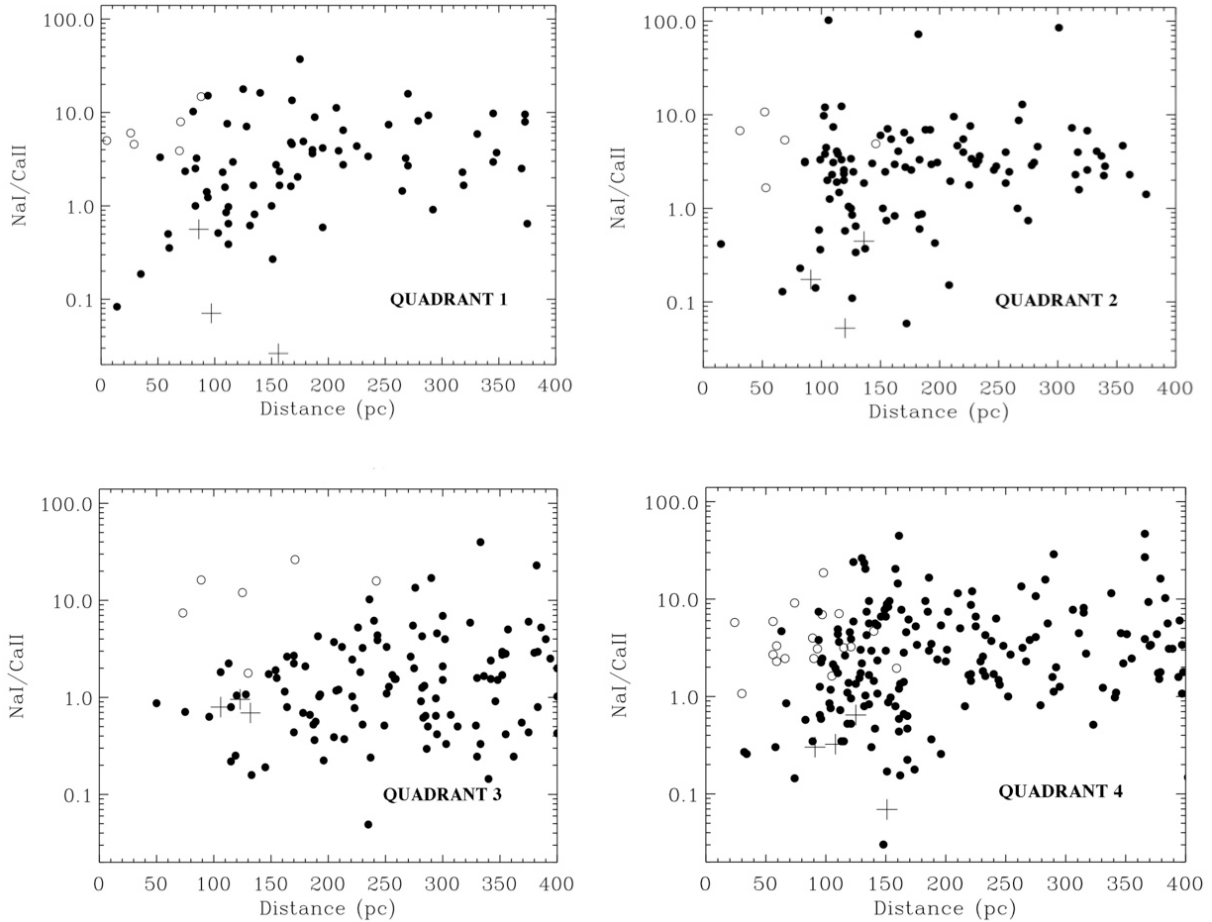


Fig. 18. Plots of the column density ratio of $N(\text{NaI})/N(\text{CaII})$ as a function of sight-line distance for galactic quadrants 1–4. Black circles are measured values, open circles are upper limits and crosses are lower limits.

in quadrant 3. This is most probably due to the presence of significant amounts of partially ionized CaII gas in the 200 pc long low neutral density interstellar tunnel seen towards the stars β and ϵ CMA which shows an ionization gradient in this galactic direction (Wolff et al. 1999).

7. Conclusion

We have presented new high spectral resolution absorption observations of the interstellar NaI D-lines (5890 Å) recorded along 482 sight-lines, together with 807 new measurements of the CaII K-line (3933 Å). When combined with existing data in the literature, we have compiled a catalog of absorption measurements towards a total of 1857 early-type stars located within 800 pc of the Sun (1678 stars measured at NaI and 1267 stars measured at CaII). By measuring both the NaI and CaII interstellar line equivalent widths and then subsequently fitting the normalized absorption profiles with a line velocity, doppler width and column density, we have been able to characterize the neutral and partially ionized properties of the interstellar medium along each sight-line. A plot of the equivalent width of NaI D2-line versus distance reveals a central region of very low neutral gas absorption ($W_\lambda(\text{D2}) < 5 \text{ m}\text{\AA}$) out to a distance of 80 pc in most galactic directions. This is the well-known Local Cavity region, which has a wall of neutral NaI gas (of $W_\lambda(\text{D2}) > 50 \text{ m}\text{\AA}$) beyond 80 pc in most directions. In contrast, a similar plot for the equivalent width of CaII shows no sharply increasing absorption

at 80 pc, but instead we observe a slowly increasing value of CaII equivalent width with increasing sight-line distance sampled.

Low values for the volume density of NaI ($n_{\text{NaI}} < 10^{-9} \text{ cm}^{-3}$) are generally found within 50 pc of the Sun (i.e. within the Local Cavity), whereas values in the range $10^{-8} > n_{\text{NaI}} > 10^{-10} \text{ cm}^{-3}$ are found for sight-lines with distance > 300 pc. Both high and low values of the volume density of CaII (n_{CaII}) are found for sight-lines < 30 pc, dependent on whether local gas cloudlets are encountered. For distances > 100 pc a value of $n_{\text{CaII}} \sim 10^{-9} \text{ cm}^{-3}$ is typical for most sight-lines, suggesting that the density distribution of CaII gas absorption is fairly uniform throughout the general ISM.

Each of the normalized absorption profiles of the NaI and CaII lines were then subsequently fit with models of line component velocity, doppler width and column density, with the total integrated values of column density for each ion along each sight-line being presented in Table 1. These new data were then used in conjunction with previous absorption measurements published in the literature to construct 3D maps of the spatial distribution of neutral NaI and partially ionized CaII gas density. This was achieved from the inversion of each column-density determination using a method based on the work of Vergely et al. (2001). The NaI maps extend and improve upon the accuracy of similar maps constructed by Lallement et al. (2003), whereas the CaII maps are the first of their kind to be published.

The general appearance of the maps of the 3D spatial distribution of NaI gas density are similar to those of CaII absorption, in that we find a ~ 80 pc diameter central region of low

absorption (i.e. the Local Cavity) surrounded by a wall of high absorption density. In contrast to the preliminary maps of NaI absorption presented in Paper I, the surrounding wall of NaI (and CaII) absorption is now found to be highly fragmented with several new interstellar tunnels of low gas density emanating from the central LC region. This fragmentation could be linked to the origin of the LC, which is generally thought to have been formed by a SN explosion over several million years ago. For most sight-lines many regions of high NaI absorption are spatially matched by regions of high CaII absorption. However, there are several important differences within the details of these maps. Firstly, the central region of the Local Cavity contains several clouds of high CaII gas density, in contrast to the general absence of neutral NaI gas clouds found within the rarefied cavity. The observed pattern of local CaII absorption appears to be in the form of a collection of several very low density interstellar cells that are surrounded by partially ionized CaII filaments. This collection of low density cavities might be caused by the combined action of stellar winds from nearby early B-type stars that could be responsible for the photoionization of the local interstellar gas. Secondly, although there are low gas density pathways that lead from the LC into the overlying galactic halo, the low density neutral NaI gas openings are of far larger dimensions than their low density CaII equivalents. Thirdly, there are several regions of high NaI absorption that do not have high CaII absorption counterparts, and vice-versa. This is reflected in the value of the integrated column density ratio of NaI/CaII for these clouds, which is presumably influenced by the ambient level of ionization in these regions.

Plots of the integrated column density ratio of NaI/CaII as a function of distance for sight-lines near to the galactic plane have values that lie in the range 0.1 to 1.0 for sight-lines with distances <80 pc. However, ratio values of between 0.5 and 20 are typical for more distant sight-lines. The highest values of the NaI/CaII ratio are found towards $l \sim 150^\circ$ in the direction of the Taurus dark clouds, and ratio values in the narrower range of 0.1 to 5 are found in galactic quadrant 3 due to the presence of the low neutral density β CMa interstellar tunnel.

Acknowledgements. We particularly acknowledge the dedicated team of engineers, technicians, and research staff at the Observatoire de Haute Provence, Mt. John Observatory, European Southern Observatory, South African Astronomical Observatory and the Lick Observatory. The observations recorded at the European Southern Observatory were taken as part of the Large Programs 077.C-0575 and 179.c-0197. This publication makes use of data products from the SIMBAD database, operated at CDS, Strasbourg, France. We also thank Christopher Henderson (University of Canterbury, Christchurch, NZ) for his help in making observations and Dr. Seth Redfield for providing us with his high resolution CaII K-line results prior to their publication in the literature. We acknowledge the effort of Jonathan Wheatley who made many of the figures for this paper and thank the referee for his comments which greatly improved the Paper. B.Y.W. acknowledges funding for this research through the NSF award AST-0507244.

References

- Albert, C. 1983, *ApJ*, 272, 509
 Albert, C., Blades, J., Morton, D., et al. 1993, *ApJS*, 88, 81
 Allen, M. 1994, *ApJ*, 424, 754
 Barlow, M. J. 1978, *MNRAS*, 183, 417
 Barstow, M., Boyce, D., Barstow, J., et al. 2009, *Ap&SS*, 320, 91
 Bates, B., Gilheany, S., & Wood, K. 1991, *MNRAS*, 252, 600
 Bates, B., Shaw, C., Kemp, S., et al. 1995, *ApJ*, 444, 672
 Benjamin, R., Venn, K., Hiltgen, D., & Sneden, C. 1996, *ApJ*, 464, 836
 Berkhuijsen, E. 1973, *A&A*, 24, 143
 Bertin, P., Lallement, R., Ferlet, R., & Vidal-Madjar, A. 1993, *A&A*, 278, 549
 Breitschwerdt, D. 2001, *Ap&SS*, 276, 163
 Bruhweiler, F., & Cheng, K.-P. 1988, *ApJ*, 335, 188
 Cardelli, J., & Wallerstein, G. 1986, *ApJ*, 302, 492
 Centurion, M., & Vladilo, G. 1991, *ApJ*, 372, 494
 Cha, A., & Sembach, K. 2000, *ApJS*, 126, 399
 Cha, A., Sahu, M., Moos, H. W., & Blaauw, A. 2000, *ApJS*, 129, 281
 Cohen, J. 1973, *ApJ*, 186, 149
 Cohen, J. 1974, *ApJ*, 194, 37
 Cohen, J. 1975, *ApJ*, 197, 117
 Combet, C., Maurin, D., Donnelly, J., O'Connell, L., & Vangioni-Flam, E. 2005, *A&A*, 435, 151
 Corradi, W., Franco, G., & Knude, J. 2004, *MNRAS*, 347, 1065
 Cox, D., & Smith, B. 1974, *ApJ*, 189, L105
 Crawford, I. 1990, *MNRAS*, 243, 593
 Crawford, I. 1991a, *A&A*, 247, 183
 Crawford, I. 1991b, *MNRAS*, 250, 707
 Crawford, I. 1992, *MNRAS*, 254, 264
 Crawford, I. 1994, *The Observatory*, 114, 288
 Crawford, I. 2000, *MNRAS*, 317, 996
 Crawford, I. 2001, *MNRAS*, 327, 841
 Crawford, I., & Dunkin, S. 1995, *MNRAS*, 273, 219
 Crawford, I., Barlow, M., & Blades, J. 1989, *ApJ*, 336, 212
 Crawford, I., Craig, N., & Welsh, B. Y. 1997, *A&A*, 317, 889
 Crawford, I., Lallement, R., & Welsh, B. Y. 1998, *MNRAS*, 300, 1181
 Crawford, I., Lallement, R., Price, R., et al. 2002, *MNRAS*, 337, 720
 Crinklaw, G., Federman, S., & Joseph, C. 1994, *ApJ*, 424, 748
 Crutcher, R., & Lien, D. 1984, in *Local Interstellar Medium*, ed. Y. Kondo, F. Bruhweiler, & B. Savage, NASA CP-2345, IAU Colloq., 81
 Dupin, O., & Gry, C. 1998, *A&A*, 335, 661
 ESA 1997, *The Hipparcos and Tycho catalogues*, ESA SP-120
 Federman, S., Knauth, D., Lambert, D., & Andersson, B.-G. 1997, *ApJ*, 489, 758
 Ferlet, R., Vidal-Madjar, A., & Gry, C. 1985, *ApJ*, 298, 838
 Franco, G. 2000, *MNRAS*, 315, 611
 Frisch, P., Sembach, K., & York, D. 1990, *ApJ*, 364, 540
 Genova, R., & Beckman, J. 2003, *ApJS*, 145, 355
 Genova, R., Beckman, J., Bowyer, S., & Specer, T. 1997, *ApJ*, 484, 761
 Grant, C., & Burrows, D. 1999, *ApJ*, 516, 243
 Gredel, R., van Dishoeck, E., & Black, J. 1993, *A&A*, 269, 477
 Hearty, T., Fernandez, M., Alcalá, J., et al. 2000, *A&A*, 357, 681
 Heiles, C. 1998, *ApJ*, 498, 689
 Hempel, M., & Schmitt, J. 2003, *A&A*, 408, 971
 Henderson, C., Welsh, B. Y., & Hearnshaw, J. 2008, *Ap&SS*, 315, 1
 Hobbs, L. M. 1974, *ApJ*, 191, 381
 Hobbs, L. M. 1975, *ApJ*, 202, 628
 Hobbs, L. M. 1978, *ApJ*, 222, 491
 Hobbs, L. M. 1984, *ApJS*, 56, 315
 Hobbs, L. M., Blitz, L., & Magnani, L. 1986, *ApJ*, 306, L109
 Hobbs, L. M., Blitz, L., Penprase, B., et al. 1988, *ApJ*, 327, 356
 Hunter, I., Smoker, J., Keenan, F., et al. 2006, *MNRAS*, 367, 1478
 Keenan, F., Dufton, P., McKeith, C., & Blades, J. 1983, *MNRAS*, 203, 963
 Keenan, F., Conlon, E., Brown, P., & Dufton, P. 1988, *A&A*, 192, 295
 Kemp, S., Bates, B., Beckman, J., et al. 2002, *MNRAS*, 333, 561
 Kennedy, D., Bates, B., & Kemp, S. 1996, *A&A*, 309, 109
 Knauth, D., Federman, S., Pan, K., et al. 2001, *ApJS*, 135, 201
 Koutroumpa, D., Acero, F., Lallement, R., Ballet, J., & Kharchenko, V. 2007, *A&A*, 475, 901
 Koutroumpa, D., Lallement, R., Raymod, J., & Kharchenko, V. 2009, *ApJ*, 696, 1517
 Lagrange-Henri, A., Ferlet, R., Vidal-Madjar, A., & Beust, H. 1991, *A&A*, 246, 507
 Lallement, R., & Bertin, P. 1992, *A&A*, 266, 479
 Lallement, R., Vidal-Madjar, A., & Ferlet, R. 1986, *A&A*, 168, 225
 Lallement, R., Bertin, P., Chassefiere, E., & Scott, N. 1993, *A&A*, 271, 734
 Lallement, R., Ferlet, R., Lagrange, A., Lemoine, M., & Vidal-Madjar, A. 1995, *A&A*, 304, 461
 Lallement, R., Welsh, B. Y., Vergely, J. L., et al. 2003, *A&A*, 411, 447 (Paper I)
 Lallement, R., Raimond, S., Redfield, S., & Welsh, B. Y. 2010, *A&A*, in preparation
 Lehner, N., Sembach, K., Lambert, D., et al. 1999, *A&A*, 352, 257
 Lehner, N., Gry, C., Jenkins, E., et al. 2003, *ApJ*, 595, 858
 Lilienthal, D., Meyerdirks, H., & de Boer, K. 1990, *A&A*, 240, 487
 Lilienthal, D., Wennmacher, A., Herbstmeier, U., & Mebold, U. 1991, *A&A*, 250, 150
 Lilienthal, D., Hirth, W., Mebold, U., & de Boer, K. 1992, *A&A*, 255, 323
 Lyons, M., Bates, B., & Kemp, S. 1994, *A&A*, 286, 535
 Megier, A., Strobel, A., Bondar, A., et al. 2005, *ApJ*, 634, 451
 Meyer, D., & Blades, J. 1996, *ApJ*, 464, L179
 Meyer, D., Lauroesch, J., Heiles, C., et al. 2006, *ApJ*, 650, L67
 Morton, D., & Blades, J. 1986, *MNRAS*, 220, 927
 Oegerle, W., Jenkins, E., Shelton, R., Bowen, D., & Chayer, P. 2005, *ApJ*, 622, 377
 Pan, K., Federman, S., Cunha, K., et al. 2004, *ApJS*, 151, 313

- Penprase, B. 1993, *ApJS*, 88, 433
 Penprase, B., & Blades, J. 1992, *ApJ*, 391, 276
 Penprase, B., Lauer, J., Aufrecht, J., & Welsh, B. Y. 1998, *ApJ*, 492, 617
 Phillips, A., Pettini, M., & Gondhalekar, P. 1984, *MNRAS*, 206, 337
 Posselt, B., Popov, S., Haberl, F., et al. 2007, *Ap&SS*, 308, 171
 Price, R., Crawford, I., Barlow, M., & Howarth, I. 2001, *MNRAS*, 328, 555
 Redfield, S. 2007, *ApJ*, 656, L97
 Redfield, S. 2009, *ApJ*, in prep.
 Redfield, S., & Linksy, J. 2002, *ApJS*, 139, 439
 Redfield, S., & Linksy, J. 2008, *ApJ*, 673, 283
 Redfield, S., Kessler-Silacci, J., & Cieza, L. 2007, *ApJ*, 661, 944
 Ritchey, A., Martinez, M., Pan, K., et al. 2006, *ApJ*, 649, 788
 Routly, P., & Spitzer, L. 1952, *ApJ*, 115, 227
 Ryans, R., Sembach, K., & Keenan, F. 1996, *A&A*, 314, 609
 Sahu, M., Blades, J., He, L., et al. 1998, *ApJ*, 504, 522
 Sallmen, S., & Welsh, B. Y. 2004, *A&A*, 426, 555
 Savage, B., & Lehner, N. 2006, *ApJS*, 162, 134
 Sembach, K. R., Danks, A. C., & Savage, B. D. 1993, *A&AS*, 100, 107
 Sfeir, D. 1999, Ph.D. Thesis, University of Paris 6, France
 Sfeir, D., Lallement, R., Crifo, F., & Welsh, B. Y. 1999, *A&A*, 346, 785
 Siluk, R., & Silk, J. 1974, *ApJ*, 192, 51
 Slavin, J., & Frisch, P. 2008, *A&A*, 491, 53
 Smith, R., Edgar, R., Plucinsky, P., et al. 2005, *ApJ*, 623, 225
 Snowden, S., Egger, R., Freyberg, M., et al. 1997, *ApJ*, 485, 125
 Snowden, S., Egger, R., Finkbeiner, D., Freyberg, M., & Plucinsky, P. 1998, *ApJ*, 493, 715
 Snowden, S., Freyberg, M., Kuntz, K., & Sanders, W. 2000, *ApJS*, 128, 171
 Sonnentrucker, P., Friedman, S., Welty, D., et al. 2003, 596, 350
 Stokes, G. 1978, *ApJS*, 36, 115
 Tarantola, A., & Valette, B. 1982, *Rev. Geophys. Sp. Phys.*, 20, 219
 Vallergera, J. V. 1998, *ApJ*, 497, 921
 Vallergera, J. V., Vedder, P., Craig, N., & Welsh, B. Y. 1993, *ApJ*, 411, 729
 Vergely, J.-L., 1998, Ph.D. Thesis, CDS, Observatoire de Strasbourg
 Vergely, J.-L., Ferrero, R. F., Egret, D., & Koeppen, J. 1998, *A&A*, 340, 543
 Vergely, J.-L., Freire Ferrero, R., Siebert, A., & Valette, B. 2001, *A&A*, 366, 1016
 Welsh, B. Y. 1991, *ApJ*, 373, 556
 Welsh, B. Y., & Lallement, R. 2005, *A&A*, 436, 615
 Welsh, B. Y., & Shelton, R. 2009, *Ap&SS*, 323, 1
 Welsh, B. Y., Vedder, P., & Vallergera, J. V. 1990, *ApJ*, 358, 473
 Welsh, B. Y., Craig, N., Vedder, P., & Vallergera, J. V. 1994, *ApJ*, 437, 638
 Welsh, B. Y., Craig, N., & Roberts, B. 1996, *A&A*, 308, 428
 Welsh, B. Y., Sasseen, T., Craig, N., et al. 1997, *ApJS*, 112, 507
 Welsh, B. Y., Craig, N., Crawford, I., & Price, R. 1998, *A&A*, 338, 674
 Welsh, B. Y., Sfeir, D., Sirk, M., & Lallement, R. 1999, *A&A*, 352, 308
 Welsh, B. Y., Sallmen, S., Sfeir, D., & Lallement, R. 2002, *A&A*, 391, 705
 Welsh, B. Y., Sallmen, S., Jelinsky, S., & Lallement, R. 2003, *A&A*, 403, 605
 Welsh, B. Y., Sallmen, S., & Lallement, R. 2004, *A&A*, 414, 261
 Welsh, B. Y., Sallmen, S., & Jelinsky, S. 2005, *A&A*, 440, 547
 Welty, D., Hobbs, L., Blitz, L., & Penprase, B. 1989, *ApJ*, 346, 232
 Welty, D., Hobbs, L., & Kulkarni, V. 1994, *ApJ*, 436, 152
 Welty, D., Morton, D., & Hobbs, L. M. 1996, *ApJS*, 106, 533
 Wennmacher, A., Lilienthal, D., & Herbstmeier, U. 1992, *A&A*, 261, L9
 White, R. 1984, *ApJ*, 284, 685
 White, R., Allen, C., Forrester, W., et al. 2001, *ApJS*, 132, 253
 Wolff, B., Koester, D., & Lallement, R. 1999, *A&A*, 346, 969
 Wolleben, M. 2007, *ApJ*, 664, 349
 Wood, K., & Bates, B. 1993, *ApJ*, 417, 572